Sensors **2007**, *7*, 760-796

sensors

ISSN 1424-8220

www.mdpi.org/sensors

Review

Stability, Nonlinearity and Reliability of Electrostatically Actuated MEMS Devices

Wen-Ming Zhang [1,*], Guang Meng [1] and Di Chen [2]

[1] State Key Laboratory of Mechanical System and Vibration, Shanghai Jiao Tong University, 800 Dongchuan Road, Shanghai 200240, China
[2] National Key Laboratory of Micro/Nano Fabrication Technology, Shanghai Jiao Tong University, 1954 Huashan Road, Shanghai 200030, China

* Author to whom correspondence should be addressed; E-mail: wenmingz@sjtu.edu.cn.

Received: 13 April 2007 / Accepted: 22 May 2007 / Published: 31 May 2007

Abstract: Electrostatic micro-electro-mechanical system (MEMS) is a special branch with a wide range of applications in sensing and actuating devices in MEMS. This paper provides a survey and analysis of the electrostatic force of importance in MEMS, its physical model, scaling effect, stability, nonlinearity and reliability in detail. It is necessary to understand the effects of electrostatic forces in MEMS and then many phenomena of practical importance, such as pull-in instability and the effects of effective stiffness, dielectric charging, stress gradient, temperature on the pull-in voltage, nonlinear dynamic effects and reliability due to electrostatic forces occurred in MEMS can be explained scientifically, and consequently the great potential of MEMS technology could be explored effectively and utilized optimally. A simplified parallel-plate capacitor model is proposed to investigate the resonance response, inherent nonlinearity, stiffness softened effect and coupled nonlinear effect of the typical electrostatically actuated MEMS devices. Many failure modes and mechanisms and various methods and techniques, including materials selection, reasonable design and extending the controllable travel range used to analyze and reduce the failures are discussed in the electrostatically actuated MEMS devices. Numerical simulations and discussions indicate that the effects of instability, nonlinear characteristics and reliability subjected to electrostatic forces cannot be ignored and are in need of further investigation.

Keywords: MEMS, Electrostatic force, Scaling effect, Stability, Nonlinearity, Reliability.

---

1. Introduction

Although electrostatic forces have found many applications, they are seldom considered for the actuation of macro-scale structures unless very high voltages are involved [1,2]. Electrostatic forces may offer distinct advantages over more familiar actuation forces at size scales approaching microns [3]. The electrostatic principle is common in the sensing and actuating MEMS devices and there are many MEMS structures subjected to electrostatic forces [2,4].

Electrostatic MEMS is an important branch with a wide range of applications including sensing devices and actuating devices in MEMS [5]. For example, the sensing devices such as capacitive accelerometers [6] and capacitive sensors [7] are widely used. In MEMS, electrostatic forces are often used to actuate microstructures, including switches [8,9], micro-grippers [10], micro-relays [11], electrostatic motors [12,13], etc. Furthermore, electrostatic forces are extensively used both in linear and rotary motors [12-14]. For an electrostatic micro-actuator with liner motion, it has been proposed parallel, quad, and comb types of actuators. Electrostatic micro-motors are classified as top-drive, side-drive, and wobble types [12,14-15], etc. Other examples of electrostatic micro-actuators are electrostatic film actuator, insect type micro robot, and air levitated electrostatic actuator system [14]. The use of electrostatic actuation in MEMS is attractive because of the quite efficient, high energy densities and large forces available for MEMS devices in micro-scale [16]. Moreover, electrostatic actuators have advantages of inherent simplicity in their design, fast response, the ability to achieve rotary motion, and low power consumption. The fabrication of electrostatic actuators is compatible with integrated circuit (IC) processes in contrast to other actuators [2]. In addition, the most successful commercialized examples are the electrostatically actuated inkjet head applied in inkjet printers and the digital micro mirror array applied in optical scanner and digital light projectors [4].

Unfortunately, microstructures undergo large deformation when subject to electrostatic actuation and the interaction between a nonlinear electrostatic force and the coupled effects from different energy fields which may cause pull-in instability and failures (stiction, wear, dielectric changing and breakdown etc.) in many electrostatically actuated MEMS devices. As a consequence of the popularity and utility of electrostatic MEMS, many aspects of effects subject to electrostatic forces in MEMS devices have been investigated in recent years. Researchers have studied the pull-in instability [17-20], characteristics of the displacement during actuation [16,21-23], shape and location of electrodes [24-26], dynamic response and optimization of the electrostatic force [9,27], nonlinear dynamics, chaos and bifurcation of the electrostatically actuated systems and analysis methods (FEM, FDM and FCM, etc.) for evaluating the nonlinear electrostatic forces [28-32], simulation software and systems (ANSYS, ABAQUS, COULOMB, MEMCAD system and Macromodel, etc.) to simulate the dynamic behaviors [31,33-35], influence of bonding parameters (applied voltage, temperature, etc.) on the electrostatic force [36], inherent nonlinear and stiffness softened effects [4,28], failure modes and mechanisms, materials selection and reasonable design, etc. in the aspects concerning reliability [15,17,37-42] in MEMS. Without an understanding of the effects of electrostatic forces in MEMS, many phenomena of practical importance, such as instability, nonlinearity and reliability in MEMS cannot be explained scientifically, and consequently the great potential of MEMS technology could neither be explored effectively nor utilized optimally. Therefore, it is important and necessary to

investigate the dynamic characteristics of the electrostatic force and its nonlinear effects on MEMS devices in micro-scale.

In this paper, a detailed review and analysis of the important electrostatic force in MEMS, its physical model, scaling effect, stability, nonlinear dynamics and reliability are depicted. It has the following structure. In section 2, the physical model is described for the analysis of electrostatic forces usually applied in MEMS. In section 3, the scaling effect on the electrostatic force in micro-scale is probed. In section 4, pull-in instability is investigated, the effects of the effective stiffness, dielectric charging, stress gradient and temperature on the pull-in voltage are discussed and several methods to extend the controllable travel range are suggested. In section 5, the nonlinear dynamic behaviors of a system under the effects of inherent nonlinearity, stiffness softened and their coupled nonlinear characteristics are studied. Different kinds of failure modes and mechanisms and methods to reduce the failures in electrostatically actuated MEMS devices are discussed in detail in section 6. Finally, the paper is ended in section 7 with conclusions.

2. Physical model

Electrostatic forces may exist between electrically charged insulator plates or between charged insulator and conductive plates [2]. For many silicon-based microstructures in MEMS, the surface area of the microstructure is much larger than the distance between the two plates. When the electrostatic force between the two plates needs to be calculated, the plates can be considered to be infinite and regarded as a one-dimensional model. The physical model used to analyze the electrostatic force is shown in Fig. 1. Plate 1 represents the anode of a capacitor while plate 2 is regarded as the cathode. If an electrostatic potential difference exists between the two plates, a uniform electrostatic field appears in the vacuum region between them. As a result of the electrostatic field, space charge layers are generated at the two inside surfaces of the plates. The space charge has a given charge distribution $\rho(z)$ from the surface to the inner of the plates.

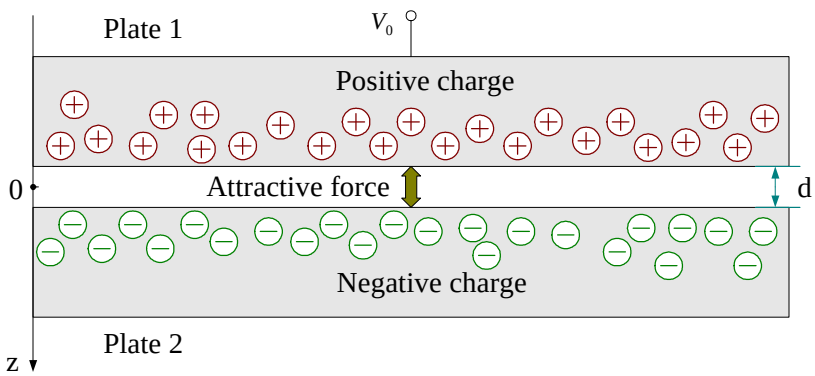

Figure 1. A physical model for analyzing the electrostatic force.

It can be considered that both plate 1 and plate 2 are n-type semiconductors [43]. If the surface electrostatic field is not very strong and the temperature is not very low, the quantum effect can be neglected. $\rho(z)$ obeys the classic Boltzmann distribution [43], thus

$$\rho(z) = q\left\{n_b\left[e^{q(V_z - V_0)/k_B T_K} - 1\right] - p_b\left[e^{-q(V_z - V_0)/k_B T_K} - 1\right]\right\} \tag{1}$$

Where q is the elementary charge, n_b and p_b are the equilibrium densities of holes and electrons, respectively, V_z is the electrostatic potential at the point z, $V_z - V_0$ is the potential difference between point z and the inside of the semiconductor plate 1, k_B is the Boltzmann constant and T_K is the temperature in Kelvin.

At the surface of one plate, one-dimensional Poisson equation can be given by

$$\frac{d^2V}{dz^2} = -\frac{\rho(z)}{\varepsilon_0 \varepsilon_r} \tag{2}$$

Where ε_0 and ε_r are the permittivity of vacuum and the relative permittivity of the material, respectively. The electrostatic field can then be obtained [43]

$$E_f(z) = \sqrt{2}\left(\frac{k_B T_K}{q}\right)\left(\frac{\varepsilon_0 \varepsilon_r k_B T_K}{q^2}\right)^{-1/2}\left\{n_b\left[e^{\frac{q(V_z - V_0)}{k_B T_K}} - \frac{q(V_z - V_0)}{k_B T_K} - 1\right] - p_b\left[e^{\frac{-q(V_z - V_0)}{k_B T_K}} + \frac{q(V_z - V_0)}{k_B T_K} - 1\right]\right\}^{1/2} \tag{3}$$

After the electrostatic field is found, the electrostatic force can be easily calculated by

$$F_e = \frac{1}{2}\varepsilon_0 A E_f{}^2 \tag{4}$$

Where E_f is the electrostatic field, A is the surface area of the plates.

3. Scaling effect

It is useful to understand how forces scale in the design of micro-sensors and micro-actuators [14, 44-45]. To explain the scaling effects on electrostatically actuated MEMS devices, Trimmer's analysis of the scaling of a simple parallel plate capacitor can be followed [44]. The size of the system is represented by a single scale parameter L, which describes the linear scaling of the system and the choice of it for a system is arbitrary. However, all dimensions of the system are equally scaled down in size as L is decreased if L is chosen. Table 1 shows the dimensions of several forces in micro-scale [14,45]. As shown in Table 1, each force has different dimension, and is affected differently by miniaturization.

Electrostatic forces become significant in micro-domain and have numerous potential applications in MEMS. The exact form of the scaling of electrostatic forces depends upon how the E_f field changes with size. Generally speaking, the breakdown electric field E_f of the insulator increases as the system becomes smaller. For the constant electric field ($E_f = [L^0]$) the electrostatic force scales as $[L^2]$. When E_f scales as $[L^{-1/2}]$, then the electrostatic force has the even better scaling of $F = [L^1]$.

Since electrostatic forces are generated between the approaching objects, there is no application for the conventional actuator except for the micro-actuator in MEMS [14]. In MEMS, electrostatic forces influence the objects effectively when they approach each other gradually. Because of that and the

scaling effect, an electrostatic micro-actuator is suitable for actuation and is easy to miniaturize. However, the issue of using the electrostatic force as the driving force is that high voltage is needed to generate it.

Electrostatic force F_e can be obtained from Equation (4) and is represented by the following formulation listed in Table 1.

$$F_e = \frac{1}{2}\varepsilon_0 A \frac{V^2}{d^2} \tag{5}$$

Where V is the applied voltage, d is the distance of gap between the two plates. Dimension of Equation (5) can be represented by

$$[F_e] = \left[\frac{1}{2}\varepsilon_0 A \frac{V^2}{d^2}\right] = \left(\frac{1}{2}\varepsilon_0 V^2\right)\cdot\frac{[L^2]}{[L^2]} = \left(\frac{1}{2}\varepsilon_0 V^2\right)\cdot\left[L^0\right] \tag{6}$$

Table 1. Scaling effects on the dimension for different kinds of forces.

Force	Formulation	Scaling	Description
Electrostatic force	$F_e = \frac{1}{2}\varepsilon_0 A E_f{}^2$	$[L^2]$	E_f : electric field strength ε_0 : permittivity A : surface area (Normal)
	$F_e = \frac{1}{2}\varepsilon_0 A \frac{V^2}{d^2}$	$[L^0]$	V : applied voltage d : gap (MEMS)
Electromagnetic force	$F_m = \frac{B^2}{2\mu_0} A_c$	$[L^2]$	μ_0 : permeability B : magnetic density A_c : area of cross section of coil
Piezoelectric force	$F_p = EA\frac{\Delta L(E)}{L}$	$[L^2]$	L : length E : Young's modules ΔL : strain
Lorentz force	$F_L = I(L \times B)$	$[L^2]$	I : current density
Thermal expansion force	$F_t = EA\frac{\Delta L(T)}{L}$	$[L^2]$	L : length E : Young's modules ΔL : strain T : temperature
Inertial force	$F_i = m\frac{\partial^2 x}{\partial t^2}$	$[L^3]$	m : mass t : time x : displacement
Viscosity force	$F_v = c_v \frac{A}{L}\frac{\partial x}{\partial t}$	$[L^2]$	c_v : viscosity coefficient A : surface area t : time x : displacement
Elastic force	$F_{el} = EA\frac{\Delta L}{L}$	$[L^2]$	L : length E : Young's modules ΔL : strain A : cross section area
Friction force	$F_f = \mu N$	$[L^2]$	μ : friction coefficient N : normal force

From Equation (5), it is noticed that it is the electrostatic field rather than high applied voltage that is responsible for the effect of the electrostatic force. In small volume, extremely high electrostatic field can be obtained, though the total voltage drop may be deceptively small [2]. Equation (6) shows that electrostatic force is generated in proportion to A/d^2, i.e. $[L^0]$. If A/d^2 is a constant in miniaturizing the electrostatically actuated MEMS devices, the electrostatic force generated has no change. Therefore, the electrostatic force can be suited as the driving force for the micro-actuators in MEMS.

A large displacement in an electrostatic micro-actuator element can be achieved only if the actuator moves parallel to the capacitor plate. The electrostatic force between the two plates includes two parts in two directions, i.e. the perpendicular electrostatic force (F_{ep}) and the tangential electrostatic force (F_{et}), can be given by [45]

$$F_{ep} = \frac{1}{2}\varepsilon_0 \frac{abV^2}{d^2} = \frac{1}{2}\varepsilon_0 A E_f^{\ 2} \tag{7}$$

and

$$F_{et} = \frac{1}{2}\varepsilon_0 \frac{bV^2}{d} = \frac{1}{2}\varepsilon_0 b d E_f^{\ 2} \tag{8}$$

Where a and b are the lateral dimensions of the poles.

These forces depend on the voltage that can be put across the electrodes. On a macroscopic level, the breakdown strength of a gas is assumed to be constant and is about $30kV/cm$ for air at room temperature and atmospheric pressure [45]. When scaled, the electrostatic force will change with a factor $[L^2]$ (the electric field is supported to be constant). At very small distances, the breakdown voltage even increases again. At atmospheric pressure, the minimum breakdown voltage is $350V$ at $8\mu m$ [45].

4. Stability analysis

4.1. Pull-in effect

A major problem is the well-known pull-in instability resulted from electrostatic forces, which tends to limit the stable travel range of many electrostatic micro-sensors and micro-actuators [16, 18, 46]. Pull-in voltage is one of the basic parameters in the design of many electrostatically actuated MEMS devices [5, 18]. In order to illustrate this phenomenon, a simplified typical variable capacitor model for the analytical description of electrostatically micro-actuators is shown in Fig. 2.

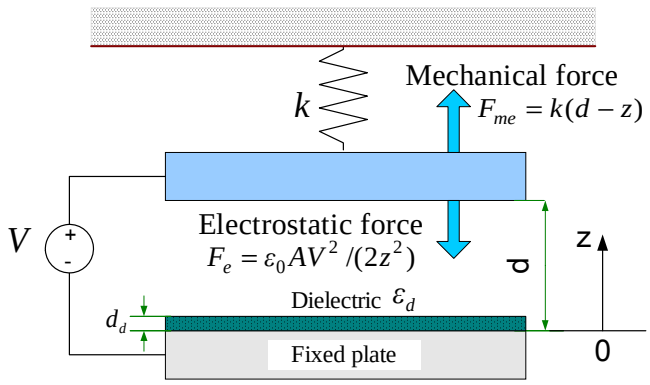

Figure 2. One-dimensional parallel-plate electrostatic micro-actuator with the mechanical force.

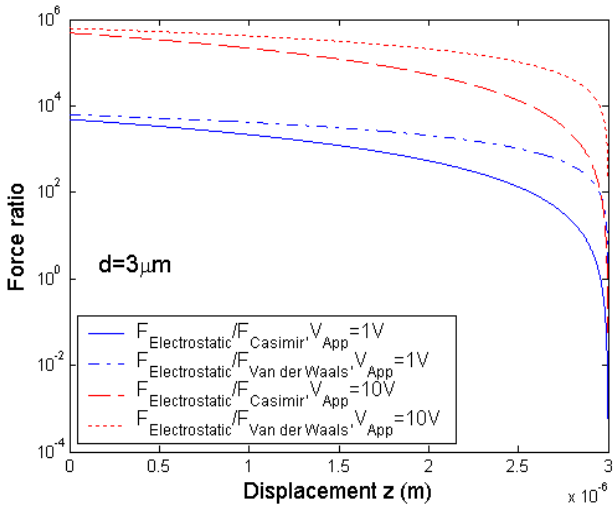

Figure 3. Comparison of the electrostatic, Casimir and Van der Waals forces for various applied voltages.

It is noted that there exist various surface forces due to the small gap between the two plates. Possible nonlinearities in the system come from the electrostatic, Casimir and Van der Waals forces. The nonlinear forces are compared in Fig. 3. At the initial gap $d = 3\mu m$, the force ratios between the electrostatic force and Casimir force and Van der Waals force become very larger when the applied voltages are $1V$ and $10V$ on the log coordinates. It is indicated that the effects of the Casimir and Van der Waals forces are smaller than the electrostatic force on the dynamic system and they can be ignored.

As illustrated in Fig. 2, the system consists of two parallel plates separated by gap z with the fixed plate on the substrate and the other suspended by a mechanical force. If the dielectric does not exist and the fringing effects is neglected, the electrostatic force can be obtained from Equation (5) and can be given by

$$F_e = \frac{1}{2}\varepsilon_0 A \frac{V^2}{z^2} \tag{9}$$

The electrostatic force is nonlinear because it depends on $1/z^2$, while the elastic restoring force, $F_{me} = k(d-z)$, is linear with z, where k is the stiffness of the spring.

The distance z at different voltages is obtained from the balance between the electrostatic force and the mechanical force, i.e. $F_e = F_{me}$, then it satisfies

$$z^3 - dz^2 + \frac{\varepsilon_0 A V^2}{2k} = 0 \tag{10}$$

From Equation (10), we can set it in the inverse form and give the following equation

$$V(z) = \sqrt{\frac{2k}{\varepsilon_0 A} z^2 (d-z)} \tag{11}$$

Analyzing Equation (11), we can obtain that the function $V(z)$ reaches its maximum value $V_{pull-in}$ at $z = z_{pull-in} = 2d/3$, i.e.

$$V_{pull-in} = \sqrt{\frac{8k}{27\varepsilon_0 A} d^3} \tag{12}$$

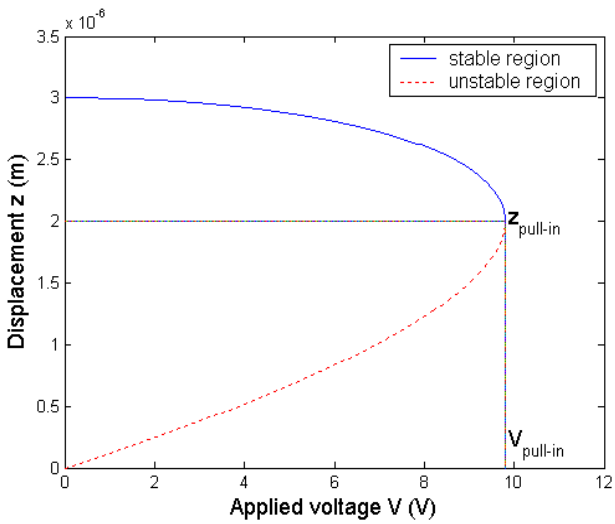

Figure 4. Electrostatic micro-actuator deflection as a function of the applied voltage.

With the values of k and d, which the reference state is $\varepsilon_0 = 8.85\times10^{-12} F/m$, $k = 0.17 N/m$, $d = 3\mu m$, $A = 1.6\times10^{-9} m^2$ [28,29], the pull-in voltage is calculated as $V_{pull-in} = 9.8V$. Fig. 4 displays the relationship between the electrostatic deflections and the applied voltages. For voltages $V < V_{pull-in}$ (i.e., at distance $z > z_{pull-in}$) the upper plate resides in a stable region. For $V > V_{pull-in}$ (i.e., at distance $z < z_{pull-in}$) the elastic suspended plate collapses towards the opposite plate, and resides in the unstable region.

Pull-in instability occurs as a result of the fact that the electrostatic force increases nonlinearly with decreasing gap ($F_e \propto z^{-2}$), whereas the mechanic force is a linear function of the change in the gap ($F_{me} \propto (d - z)$). The equilibrium position of the plate may be found by equaling the electrostatic and mechanical forces. As V increases, the gap distance at first decreases gradually. However, at a critical voltage value (i.e. pull-in voltage), a bifurcation occurs, and the plate suddenly collapses. The maximum stable deflection of the plate before pull-in is 1/3 of the undeflected gap d.

4.2. Effects on the pull-in voltage

4.2.1. Effect of effective stiffness k_{eff}

The analysis for estimating effective stiffness k_{eff} of the spring is simplified to a large range due to the absence of axially induced forces [5]. A micro-cantilever beam is subjected to a distribution load over a partial length L_p originating from the tip of the beam. The stiffness of the spring seen at the point of the maximum displacement [5], i.e. at the free end, is easily evaluated and is given by

$$k_{eff} = \frac{2}{3}\frac{E^* bh^3}{L^3}\left(\frac{3}{8 - 6\lambda_r + \lambda_r^{\,3}}\right) \tag{13}$$

Where $\lambda_r = L_p / L$, b, h and L are the width, depth and length of the micro-cantilever beam, respectively. The effective Young's modulus E^* is equal to E for $b \approx h$, and equal to the plate modulus $E/(1-\upsilon^2)$ for $b > 5h$, υ is the Poisson ratio.

The influence of partial load on the pull-in voltage is shown in Fig. 5 for a polysilicon micro-cantilever beam with $E = 160GPa$, $\upsilon = 0.27$, $b = 50\mu m$, $h = 1\mu m$ and $d = 3\mu m$. As the beam length increases, the pull-in voltage is becoming smaller. It is noted that $V_{pull-in}(\lambda_r = 0.1) >_{pull-in} (\lambda_r = 0.3) > V_{pull-in}(\lambda_r = 0.5) > V_{pull-in}(\lambda_r = 1)$ for the same beam length. This is because k_{eff} gradually reduces as λ_r is varying from 1 to 0.1.

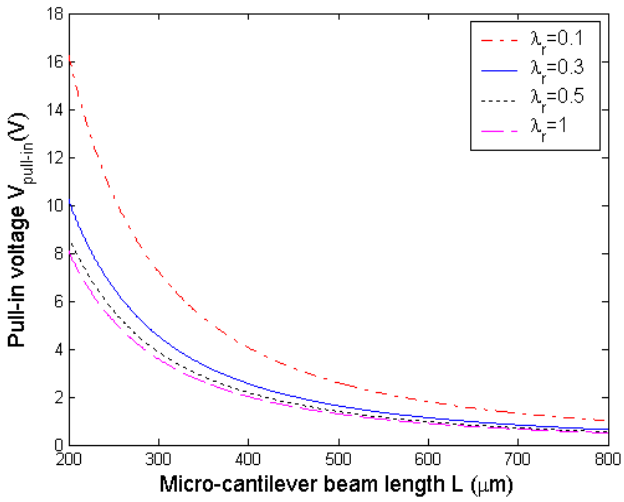

Figure 5. Pull-in voltage versus micro-cantilever beam length for various λ_r ($E = 160GPa$, $\upsilon = 0.27$, $b = 50\mu m$, $h = 1\mu m$, $d = 3\mu m$).

4.2.2. Effect of dielectric charging

If the effect of the interfacial charge σ_p at the air dielectrics interface in the electrostatically actuated model shown in Fig. 2 has been considered, it has been proven that the pull-in voltage of the cantilever beam will have to increase to compensate for the field reduction in the air gap due to the interface charge. The voltage offset V_{offset} due to the parasitic charge can be expressed as [47]

$$V_{offset} = -\frac{\sigma_p}{\varepsilon_d} d_d \tag{14}$$

This offset is best determined by calculating half the difference between the absolute values of the positive and negative pull-in voltage. Thus, sensors and actuators are subject to an additional electrostatic force depending nonlinearly on the applied voltage and the displacement. The pull-in voltage with the effect of the interface charge can be given by [48]

$$V_{pull-in} = \sqrt{\frac{2k}{3\varepsilon_0 A}\left(\frac{2}{3}d + \frac{d_d}{\varepsilon_d}\right)^2 d} \tag{15}$$

Where d_d, ε_d are the thickness and the relative permittivity of the dielectric, respectively.

It is indicated that the effect of the interface charge is to shift the pull-in voltage. The increase of the pull-in voltage can be explained by the accumulation of charges in the dielectric. They create a parasitic electric field that superposes the electric field created by the applied actuation voltage.

4.2.3. Effect of stress gradient

The release of a cantilever beam from the substrate can lead to an important beam curvature if stress is not homogenous over the thickness direction. This gradient of stress over the thickness direction causes a moment that results in a maximum deflection, the deflection can be written as [49]

$$z_{\max} = \frac{L^2 \Delta\sigma}{2E} \tag{16}$$

Where $z_{\max}$ is the maximum beam deflection, σ is the stress. The deflection of the micro-cantilever beam can be easily measured by optical profilometers or microscopes.

Rocha et al. [50] introduced the in plane $0.2 MPa/\mu m$ stress gradient in the actuator capacitor model to check its effect on the pull-in voltage. Since the stress gradient causes bending, the electrostatic force is not in equilibrium and there is a small initial deflection of the micro-cantilever beam. In this case, the pull-in voltage shifts to a lower value than that previously calculated.

4.2.4. Effect of temperature

The pull-in voltage shows a temperature coefficient [50]. The source of the temperature dependence of the pull-in voltage appears to be the thermal expansion of the materials and the dependence of

Young's modulus on the temperature. Both properties change the mechanical spring of the system, leading to changes in the voltage required to get the critical deflection.

If a simple analysis is performed concerning the thermal effect on the micro-cantilever beam, the spring stiffness k is represented as the temperature dependent part [51]. The relationship between the temperature T and the spring stiffness k can be expressed as

$$k(T) = k\left[1 + (\alpha + \beta)T\right] \tag{17}$$

Where α and β are the thermal expansion coefficient and the Young's modulus thermal coefficient, respectively. For the polysilicon structure, the thermal expansion coefficient is $\alpha = 3\times10^{-6}K^{-1}$ and the Young's modulus thermal coefficient is $\beta = -67\times10^{-6}K^{-1}$ [50,51].

Substituting Equation (17) into Equation (12) and taking the derivative to temperature, the following expression can be yielded by

$$\frac{\partial V_{pull-in}}{\partial T} = \sqrt{\frac{8k}{27\varepsilon_0 A}d^3} \cdot \frac{\alpha+\beta}{2\left[1+(\alpha+\beta)\right]^{1/2}} = V_{pull-in} \cdot \frac{\alpha+\beta}{2\left[1+(\alpha+\beta)\right]^{1/2}} \tag{18}$$

From Equation (18), it can be seen that the pull-in thermal efficient is nonlinear, and that it increases with the temperature. For example, there are two opposite effects acting on the pull-in voltage of the RF switch [49]. Firstly, the bridge dilates with the increase of temperature, the gap increases and thus also the pull-in voltage. Secondly, the Young's modulus decreases with increasing temperature, therefore the bridge's stiffness and consequently the pull-in voltage decrease. Rocha et al. [52] presented a two DOF analytical pull-in model to verify the effect of the temperature on the pull-in voltage. Introducing $\alpha = 3\times10^{-6}K^{-1}$ and $\beta = -67\times10^{-6}K^{-1}$, the relationship between the temperature and the pull-in voltage can be obtained. The pull-in voltage has been computed between 0 and $40^{\circ}C$ and yielded a $-0.5mV/K$ temperature coefficient [50]. Moreover, Tada et al. [53] reported that the Young's modulus temperature coefficient contains quadratic and higher terms in addition to the linear coefficient β.

4.2.5. Extending the travel range

Although the electrostatically actuated MEMS devices are widely used, they are inherently limited in the travel range due to stable actuation is achievable only over one third of the gap between the plates. Therefore, it is desirable to increase the travel range of the electrostatically actuated MEMS devices beyond the $1/3$ limit.

Design trade-offs have to be made between force, displacement and applied voltage requirements for extending the travel range. Several methods have been suggested to extend the controllable travel range by optimizing the structural design [16], by incorporating an on-board folded capacitor on the device [22], by using a multiphase piecewise linear mechanical flexure [54], by external electrodes [55], and by adding additional circuitry [56]. A control law was proposed in [57] for linearizing an electrostatic actuator. Sun et al. [58] presented experimental results using a nonlinear model to extend the travel range without additional hardware and device area and further complicate fabrication

processes. In attempts to extend the controllable regime for device actuation, designers have implemented a zipping approach to electrostatic design [59], also demonstrated with curved laterally displaced electrostatic cantilever devices [60]. Moreover, charge control [61], which is opposed to voltage control, becomes one effective way to extend the stable range of actuation.

For example, Hung et al. [16] investigated the pull-in instability and presented the leveraged bending and strain-stiffening methods for extending the stable travel range of electrostatic actuators beyond 1/3 of the pull-in instability limit for parallel-plate electrostatic actuators. The leveraged bending method is to reduce the pull-in instability by applying electrostatic force to only a part of a structure, then using the rest of the structure as a lever to position specific parts of the structure through a large range of motion. As shown in Fig. 6, the leveraged bending method is applied to a simple electrostatically actuated beam. In this case, the beam can move the larger gap, even if the part of the beam that is being electrostatically actuated moves 1/3 of the gap or less. The leveraged bending effect can be used to maximize the travel range of an electrostatic micro-actuator for a given gap size, achieving up to full gap travel at the cost of increased actuation voltage.

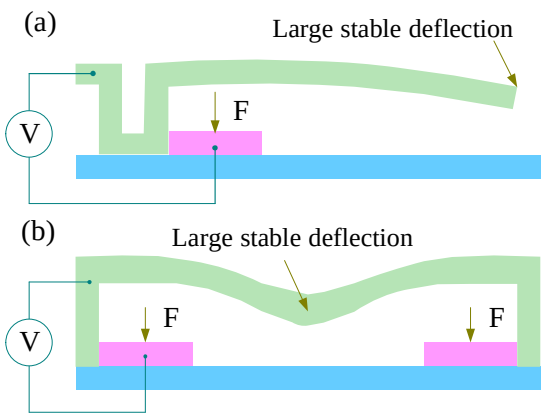

Figure 6. Leveraged bending method to extend the stable travel range of an electrostatic micro-actuator: (a) cantilever beam; (b) doubly clamped beam.

Rosa et al. [55] demonstrated the benefits of a novel external electrode scheme that allows stable operation and full analog control over the entire range of motion of the curved cantilever beams.

As displayed in Fig. 7, the counter electrodes are offset from the actuator rather than being positioned directly underneath it can lead to the stable actuation over the full range of motion. In Fig. 7(a), the electrostatic force is still proportional to the inverse square of the distance at large separations, but it reaches a maximum at a certain distance before it decreases again and becomes zero when the actuator is aligned with the counter electrodes. For the external tapered electrode shown in Fig. 7(b), the voltage-displacement characteristic is nonlinear but stable over the entire actuation range. Moreover, no notable hysteresis is observed and fine actuation control over the full range is achieved. Therefore, the external electrode configuration is an attractive alternative to the electrostatically actuated MEMS devices.

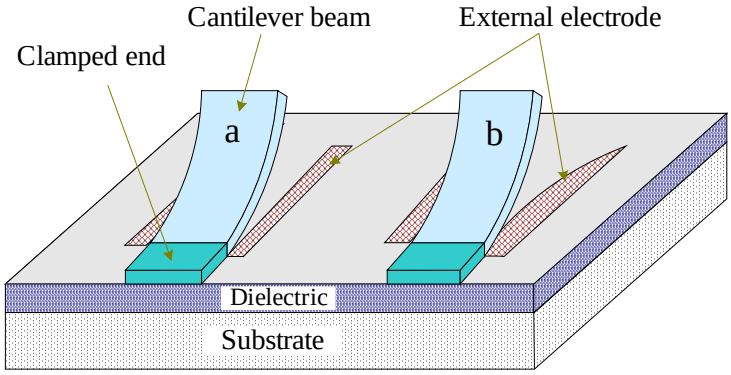

Figure 7. Schematic diagrams of the micro-cantilever beams: (a) external electrode; (b) and tapering external electrode.

5. Nonlinearity analysis

5.1. Resonance response

The electrostatic force has a square dependence on the applied voltage $V = [V_0 \cos(\omega t)]^{1/2}$, in order to isolate the parametric effects from harmonic effects, we can use a square rooted sinusoidal voltage signal. We presented a modified nonlinear Mathieu equation for the electrostatically actuated system [28] shown in Fig. 2, i.e.

$$\ddot{x} + \psi(x, \dot{x}) + x + f_0(x) + q(t) \cdot e(x) = p(t) \tag{19}$$

Where $\psi(x, \dot{x}) = \zeta \dot{x}$, $f_0(x) = 0$, $q(t) = \Psi V_0 \cos \Omega t$, $e(x) = -2x - 3x^2$, $p(t) = \Psi V_0 \cos \Omega t$, $\Omega = \omega / \omega_0$, $\zeta = c / \sqrt{km}$, $\omega_0 = \sqrt{k/m}$ and $\Psi = \dfrac{\varepsilon_0 A}{2m\omega_0{}^2 d^3}$.

Using the harmonic balance (HB) method, the relationship between the amplitude a and the dimensionless frequency a^* can be given by

$$a^2 = \left(\frac{a^* \Psi V}{\Omega^2 a^{*2} + \zeta^2}\right)^2 + \left(\frac{\Psi V_0 \Omega}{\Omega^3 a^{*2} + \Omega \zeta^2}\right)^2 \tag{20}$$

Where Ψ and ζ are the dimensional variables, Ω is the resonant parameter.

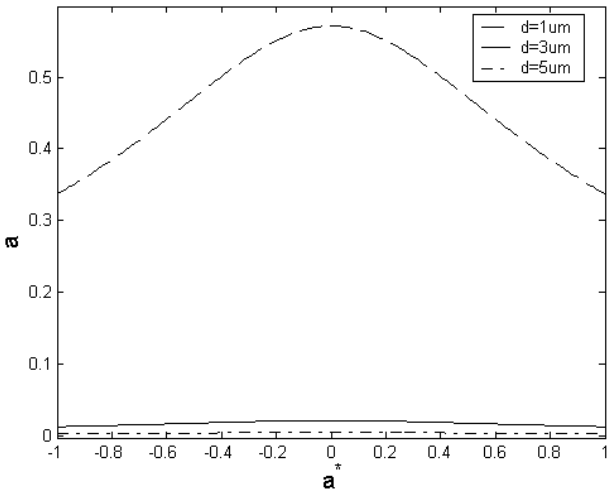

Figure 8. The relationship between the amplitude a and the frequency a^* of an electrostatically actuated system in MEMS when $d = 1um, 3um, 5um$ with $V_0 = 10V$ and $\Omega = 1$.

The relationships between the amplitude a and the frequency a^* under different applied voltages and various gaps between the plates are illustrated in Fig. 8. As showed in Fig. 8, the amplitude a reduces quickly and tends to an approximation when the gap between the plates is becoming wider (e.g., $a \approx 0.005$ at $d = 5um$ with $\Omega = 1$ and $V_0 = 10V$). Therefore, the gap d and the applied voltage V_0 are the main factors for the measurement and detection of the displacement of an electrostatically actuated system in MEMS.

5.2. Inherent nonlinear effect

It is known that the dynamic characteristics of a system depend on the operational parameters, geometrical dimensions and material properties [4]. However, for an electrostatically actuated system, the electrostatic force will change the dynamic characteristics of structures and as the structure deforms, the electrostatic force redistributes, thereby modifying the mechanical loads.

Expanding the nonlinear electrostatic force term $\varepsilon_0 A V^2/(2(d-z)^2)$ in Equation (9) by Taylor series with respect to the equilibrium position, i.e. $z = 0$, gives

$$\frac{1}{2}\varepsilon_0 A \cdot \frac{V^2}{(d-z)^2} = \frac{1}{2}\varepsilon_0 A \cdot \frac{V^2}{d^2}(1 + \frac{2}{d}z + \frac{3}{d^2}z^2 + \cdots) \tag{21}$$

Based on the small displacement assumption, the higher order terms can be neglected, thus the nonlinear electrostatic force can be linearized as

$$\frac{1}{2}\varepsilon_0 A \cdot \frac{V^2}{(d-z)^2} = \frac{1}{2}\varepsilon_0 A \cdot \frac{V^2}{d^2}(1 + \frac{2}{d}z + \frac{2}{d^2}z^2) \tag{22}$$

Introducing the dimensional vector $[x_1, x_2]^T = [x, \dot{x}]^T$, the state space representation of the electrostatically actuation model gives a nonlinear, parametric and forcing excitations, time-varying and T-periodic model, i.e.

$$\begin{bmatrix} \dot{x}_1 \\ \dot{x}_2 \end{bmatrix} = \begin{bmatrix} x_2 \\ -\zeta x_2 - x_1 + (2x_1 + 3x_1^2)\Psi V_0 \cos\Omega t + \Psi V_0 \cos\Omega t \end{bmatrix} \tag{23}$$

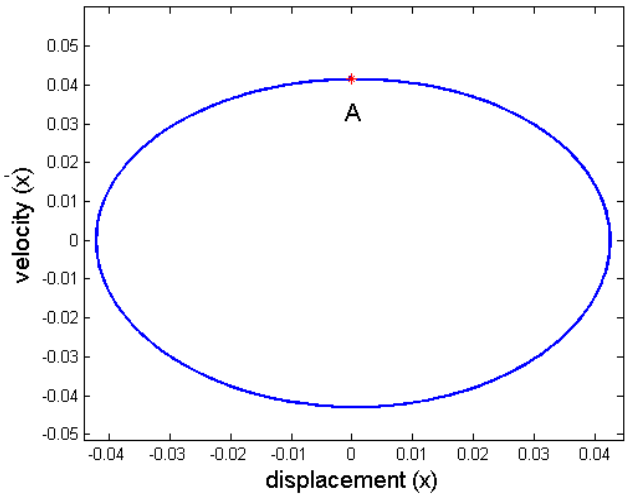

Figure 9. phase portrait and Poincare map of the nonlinear dynamic system with $V_0 = 20V$, $\Omega = 1$ and $d = 3um$, **t**he simulation is scaled in time with relation $t = \omega t_0$ for numerical integration accuracy.

The phase portrait of the system is a representation of all its trajectories. Fig. 9 illustrates the phase portrait to investigate the nonlinear dynamical behaviors of the system. It can be found that the phase portrait at $\Omega = 1$ is a two-dimensional close loop and its stable equilibrium is a fixed point A (in Poincare plane) for trajectory in phase space. Therefore, the system is stable for different resonant parameters without considering the nonlinear spring stiffness term.

5.3. Stiffness softened effect

The electrostatic force can significantly affect and soften the stiffness of a dynamic system [4, 30-31]. Adams et al. [30] utilized a combination of two or more electrostatic actuators to produce linear, quadratic, cubic, and higher order stiffness. He also carried out experiments focused on determining the electrostatic stiffness produced using different tuning voltage combinations and obtained the result that the electrostatic stiffness is roughly inversely proportional to the gap squared. Zhang et al [31] presented the modeling, analysis, and experimental verification that the nonlinear effect of the cubic electrostatic stiffness changes the dynamic behavior of the system.

To analyze the stiffness softened effect on the dynamic system, the modal expansion method [4] can be used to discretize the governing equation of the dynamic system and the modal stiffness k_j' can be obtained

$$k_j = k_j' - k_s = k_j' - \frac{\varepsilon_0 A V_0^{\,2} \cos^2(\omega t)}{d^3} - \frac{3\varepsilon_0 A V_0^{\,2} \cos^2(\omega t)}{2d^4} \tag{24}$$

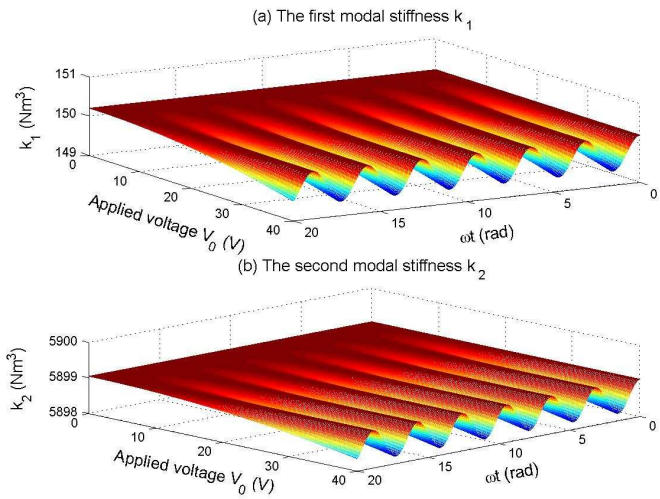

Figure 10. Changes of the first and second modal stiffness.

Equation (24) shows that the modal stiffness k_j is a periodically time-varying function depending on the applied voltage. It is indicated that the electrostatic force soften the modal stiffness of the microstructure periodically. Numerical simulations and results of the changes of the first and second modal stiffness k_1 and k_2 are illustrated in Fig. 10.

As can be seen in Fig. 10, the modal stiffness decreases periodically with the frequency ω of the applied voltage and the variation increases with the larger magnitude V_0. Therefore, the stiffness of an electrostatically actuated microstructure in MEMS will be softened periodically with the frequency of the applied voltage and the variation increases with the increasing of the magnitude of the applied voltage.

5.4. Coupled nonlinear effect

The structure-electrostatic coupling effect must be taken into account on the design of electrostatically actuated MEMS devices. MEMS devices are often characterized by structures that are a few microns in size, separated by micron-sized gaps. At these sizes, air damping dominates over other dissipation. Squeeze film damping may be used to represent the air damping experienced by the moving plates [62,63]. Starr [64] presented the expression of the damping force for a rectangular plate of dimensions $2b \times 2L$ as

$$F_{sfd} = -\frac{16\mu c_r b^3 L}{x^3}\dot{x} = -\frac{k_2}{x^3}\dot{x} \tag{25}$$

Where μ is the viscous coefficient, b and L are the width and length of the beam, respectively [29]. And c_r is approximately equal to

$$c_r = 1 - 0.6\tfrac{W}{L}, \ (0 < \tfrac{W}{L} < 1) \tag{26}$$

The applied voltage is an important factor of the parallel plate capacitor which leads to coupled nonlinearities. It is useful to understand the dynamic characteristics of the electrostatically actuated MEMS devices by the chaotic motions of the systems due to the cubic nonlinear term. Fig. 11(a)~(d) are the bifurcation diagrams of V_0 and Poincare maps at different applied voltages without the effect of squeeze film damping for the coupling system when the cubic nonlinear stiffness is $k_1 = 0.3$.

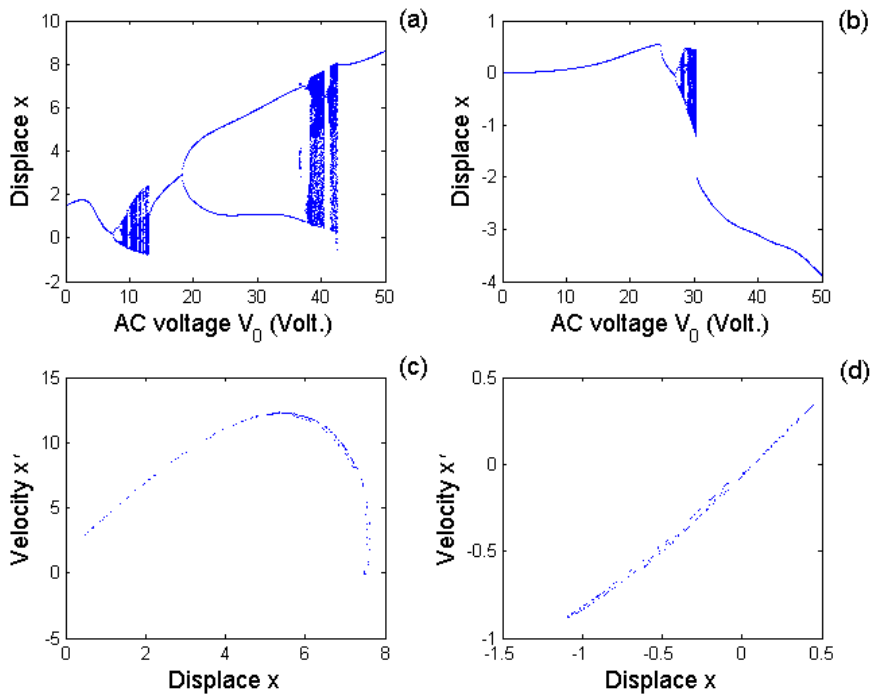

Figure 11. Bifurcation diagrams of V_0 for the electrostatic coupling nonlinear dynamic system and Poincare maps under different applied voltages: (a) Bifurcation diagram of V_0 ($V_P = 20V$); (b) Bifurcation diagram of V_0 ($V_P = 0V$); (c) Poincare map ($V_0 = 40V$, $V_P = 20V$); (d) Poincare map ($V_0 = 30V$, $V_P = 0V$).

It can be seen from Fig. 11(a) that the response of the electrostatic coupling system is stable when V_0 gets lower value. When $V_0 > 7.4V$, the system response displays double periodic bifurcation: $P-1 \to P-2 \to P-4$. Then, the system response changes between quasi-periodic and periodic motions alternatively when V_0 varies from $8.8V$ to $13.0V$. When $V_0 > 13.0V$, the system response becomes $P-1$ (period one) motion, then shows double periodic bifurcation and enters into chaotic motion, and finally leaves chaotic state with periodic one motion. Fig. 11(c) shows the Poincare map of the system response at $V_0 = 40V$. There is an isolated chaotic island in the Poincare map. It is indicated that the system is chaotic at this time. Fig. 11(b) is the bifurcation diagram of V_0 for the electrostatic coupling dynamic system at $V_P = 0V$. When $V_0 > 27.1V$, the system response shows double periodic bifurcation: $P-1 \to P-2 \to P-4$. Then, the system response alternates between quasi-periodic and periodic motions ($P-6$, $P-3$, etc) in turn when V_0 varies from $27.9V$ to $30.5V$. Fig. 11(d) illustrates the Poincare map of

the system response at $V_0 = 30V$. It is found that a closed ring formed in the Poincare map and the system is quasi-periodic. Therefore, the alternating current (AC) voltage and the polarization voltage play an important role in the system responses and the responses display very rich dynamic behaviors when these two kind of voltages change.

Squeeze film damping coefficient and ratio are the key parameters for the dynamic responses of the MEMS devices. The larger the squeeze film damping, the louder noise will exist. Considering the effect of squeeze film damping structural coupling with the electrostatic force on the system response, Fig. 12(a)~(d) display the bifurcation diagrams of the damping ratio c_g. It can be seen from Fig. 12(a) that the system response changes between periodic, quasi-periodic and chaotic motion alternatively when $c_g > 0.5$. Then it enters into $P-3$ motion from chaotic state when $c_g > 0.64$. when $c_g > 0.86$, it displays inverse double period bifurcation: $P-8 \to P-4 \to P-2 \to P-1$ and becomes $P-1$ motion. With the increase of polarization voltage, the system response changes obviously. Fig. 12(b) illustrates the bifurcation diagram at $V_P = 5V$. It is found that the system response displays inverse periodic bifurcation from $P-2$ motion to $P-1$ motion, and then enters into chaotic motion when $c_g > 0.58$. When the squeeze film damping ratio is increasing continuously, the system response changes among chaotic, periodic ($P-4$, $P-8$ and $P-3$, etc.) and quasi-periodic motions alternatively. The system response shows double periodic bifurcation ($P-2 \to P-4$) when $c_g > 0.70$. When the alternating current (AC) and polarization voltages vary simultaneously, the system responses change obviously. Fig. 12(c) and Fig. 12 (d) are the system responses for the two combinations: $V_0 = 20V$, $V_P = 30V$ and $V_0 = 30V$, $V_P = 20V$. Therefore, the effect of squeeze film damping on the system response can not be neglected for MEMS structures in micro-scale. The dynamic characteristics of the electrostatically actuated MEMS devices will alter with the change of the alternating current (AC) and polarization voltages.

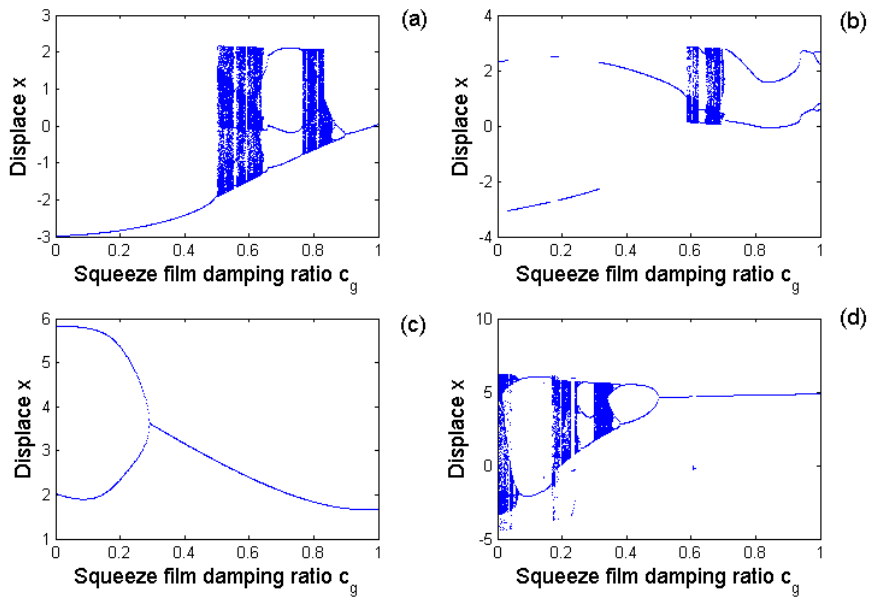

Figure 12. Bifurcation diagrams of c_g for the electrostatic coupling nonlinear dynamic system: (a) $V_0 = 40V$, $V_P = 0V$, $k_1 = 0.3$, $\Omega = 1$; (b) $V_0 = 40V$, $V_P = 5V$, $k_1 = 0.3$, $\Omega = 1$; (c) $V_0 = 20V$, $V_P = 30V$, $k_1 = 0.3$, $\Omega = 1$; (d) $V_0 = 30V$, $V_P = 20V$, $k_1 = 0.3$, $\Omega = 1$.

6. Reliability analysis

Reliability of sensing and actuating devices due to electrostatic forces is a very young and important field in MEMS. A failure is said to occur when an electrostatic microstructure or its system no longer performs the required functions under the specific conditions within the stated period of time. There have two main failures: irreversible failures and degradation failures. Fig. 13 illustrates the methodology of the reliability analysis for electrostatically actuated MEMS devices. Table 2 shows the common failure modes and mechanisms of the electrostatically actuated devices in MEMS.

Table 2. Common failure modes and mechanisms of the electrostatically actuated devices in MEMS.

Failure mode	Failure mechanism	Example	Reference
Stiction and adhesion	Surface contact	Comb finger actuator, beam	[65, 66]
Electrostatic interference	Electrical contact	Electrostatic micro-motor	[12, 15]
Dielectric changing and breakdown	Nuclear radiation	Accelerometer, RF MEMS switch	[8, 47, 67]
Wear and friction	Surface contact and rubbing	Micro-motor, microengine	[68, 69]
Fracture	Intrinsic and applied stress	comb finger actuator	[70]

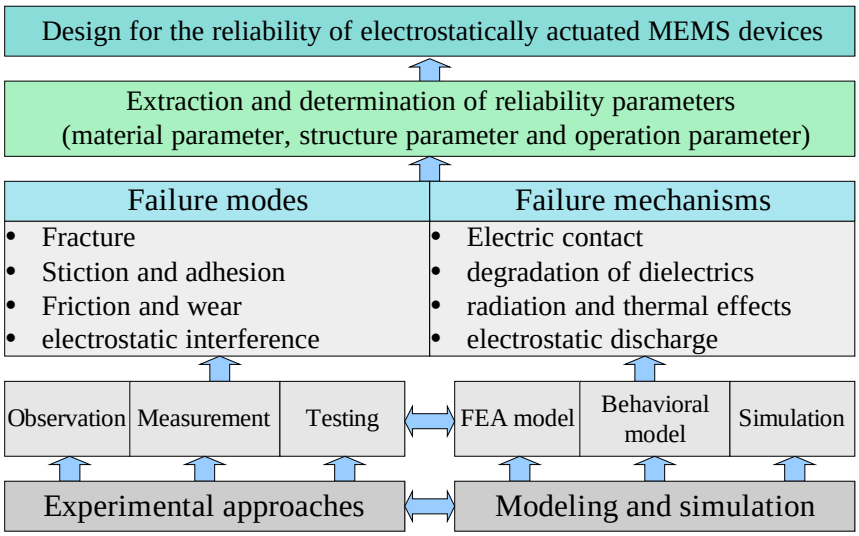

Figure 13. Methodology of reliability analysis for the electrostatically actuated MEMS devices.

6.1. Failure models and mechanisms

6.1.1. Fracture

Fracture strength, a statistical property in brittle materials such as silicon, is a function of microstructure and processing, which can exhibit variation from run to run due to process variability [71]. Stress in polysilicon elements should be kept to 10% or less of the measured fracture strength for the material and process in use. Stress values in the range of several hundred MPa appear to be quite acceptable. A completed device [70] is shown by the scanning electron micrograph SEM in Fig. 14.

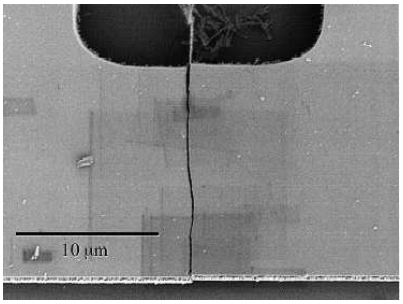

(*Courtesy of H. Kahn***)**

Figure 14. SEM micrographs of a MEMS fracture [70].

Fracture occurs when the applied load on an electrostatically actuated MEMS device is greater than the strength of the component materials. Fracture is a serious reliability concern because it can immediately cause catastrophic failures, particularly for the brittle materials. Therefore, it is very important to know the mechanical properties of the materials and microstructures in micro-scale for the electrostatically actuated MEMS devices.

6.1.2. Stiction and adhesion

Stiction is the effect that microstructures tend to adhere to each other when their surfaces come into contact [65,66]. Stiction and adhesion are the important and almost unavoidable problems that occur in the electrostatically actuated devices fabricated by surface micromachining in MEMS. Surface tension forces such as electrostatic force can pull the MEMS component into contact with the substrate resulting in stiction failure. Other causes of stiction include shock induced stiction and voltage overstress resulting in contact.

Stiction between the contact surfaces limits the repeatability of operation or may even prevent the operation completely. The components of the electrostatically actuated MEMS devices are small, therefore, the surface forces can dominate each other and cause these parts come into contact. The surface roughness is a major influence in the stiction phenomenon [66]. Permanent adhesion arises from the large interfacial forces (capillary, electrostatic, and van der Waals forces) compared with the restoring force of the deflected structure. All of these forces must be manipulated if the adhesion force is to be reduced below the mechanical restoring force.

Stiction can be prevented or reduced in several ways, which can roughly be divided into two groups: methods based upon the prevention of physical contact between structures and the substrate during

fabrication; methods based upon the reduction of adhesion forces [72]. To minimize electrostatic attraction, the two surfaces should be conductive, allowing charges to be dissipated. A reduction in the effective contact area is also necessary to further reduce the overall adhesion forces in the electrostatically actuated MEMS devices.

6.1.3. Friction and wear

Many electrostatically actuated MEMS devices involve surfaces contacting or rubbing against one and other, resulting in friction and wear [41]. The operation of micromachined devices that have contacting joints and bearings is significantly affected by friction and wear of the contact surfaces involved.

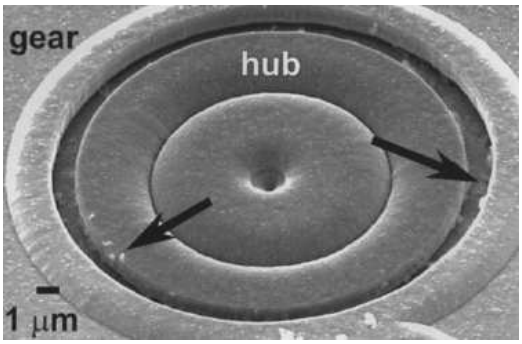

(*Courtesy of D.M. Tanner***)**

Figure 15. SEM image of characteristic wear debris on the drive gear and the hub [69].

Gabriel et a1. [68] investigated the significant wear on the hub of an electrostatic micro-motor. In the micro-motor, the rotor is driven electrostatically in the stator, but in practice because of the small clearance between the hub and the rotor, there may be existed physical contact. Tanner et al. [69] studied the wear of an electrostatically driven microengine developed at Sandia National Laboratory. Severe wear of the pin joint and wear debris near the rubbing surfaces was evident. Wear of rubbing surfaces was the dominant mode of the failure for the microengine. Fig. 15 shows the SEM image of the characteristic wear debris on the drive gear and the hub.

6.1.4. Dielectric charging and breakdown

A most important problem of MEMS devices with dielectric layers is the charging of the dielectrics [47, 72-75]. Electrostatically actuated MEMS devices commonly require high operating voltages (100~200 V) applied across a few microns gaps, resulting in electric fields as high at $10^8 V/m$ applied across the dielectric between electrodes [47,73]. The high fields in the bulk or across the surface of the dielectric can cause charge injection and leakage currents that contribute to some possible failures. With the high field strengths, conductions are governed by nonlinear conduction effects due to charge injection, conduction via traps and tunneling in dielectric, such as Schottky, Poole–Frenkel (PF) and Fowler–Nordheim (FN) conductions [72,73].

(1) Electrostatic interference

Materials with high insulation resistance and field strength, such as silicon oxide and silicon nitride, are often used for insulation in the electrostatically actuated MEMS devices. The bulk or surface of such dielectrics can be charged up locally and they provide trap sites for positive and negative charges both deep in the bulk and at the interfaces in multilayer stacks [47]. Parasitic charge accumulating in the electrostatically actuated MEMS devices may alter actuation voltages and change the mechanical behaviors. Wibbeler et al. [47] studied the effects of parasitic charges on the relationship between the deflection and applied voltage of bulk micromachined silicon cantilever actuators and provided measurements of the charge decay.

For example, schematic illustration of a RF MEMS switch with dielectric is shown in Fig. 16. The beam will move downwards when subjected to the electrostatic force due to the applied voltage. The distance between the beam and dielectric will then change. Charging can arise during handling and operation. High applied voltage exceeding the breakdown voltage of the gap will give rise to considerable charge deposition of the dielectric. When the dielectric is charged by the ionizing radiation and causes a change in position of the beam due to electrostatic actuation, the device behavior will become erratic.

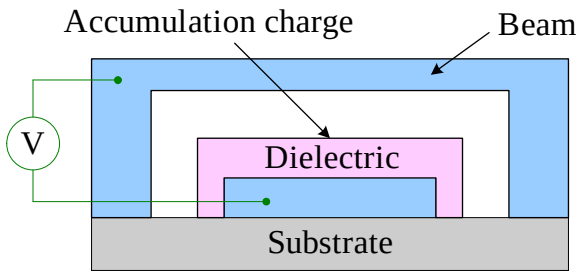

Figure 16. Schematic illustration of a RF MEMS switch with dielectric.

(2) Radiation effect

It is well-known that electrical systems are susceptible to radiation. The most obvious source of dielectric charging is ionizing radiation, which can be a major problem for the application of MEMS. Schanwald et al. [74] evaluated the mechanical and electrical performance of MEMS comb drive and microengine actuators in the total dose radiation environments. Radiation induced charging can be developed between the gear hub and the drive gear, and the gear pin and the drive gear [74]. Radiation effect can aggravate the lateral and linear electrostatic clamping failures when comb drives.

The radiation effect is attributed to electrostatic force caused by charge accumulation in dielectric layers, such as Parylene, SiO_2, Si_3N_4, etc. To illustrate the charging mechanism, a physical arrangement is shown in Fig. 17. The charge distribution in the dielectric produced by radiation in the presence of a biasing voltage is complicated due to the gap between the dielectric and the lower electrode plate [75]. As illustrated in Fig. 17(a), for negative bias during radiation, secondary electrons are emitted from the dielectric before becoming thermalized and lead to a net positive charge at the surface of the dielectric. For positive bias during radiation, secondary electrons are emitted from the lower electrode plate are attracted to the dielectric, as displayed in Fig. 17(b).

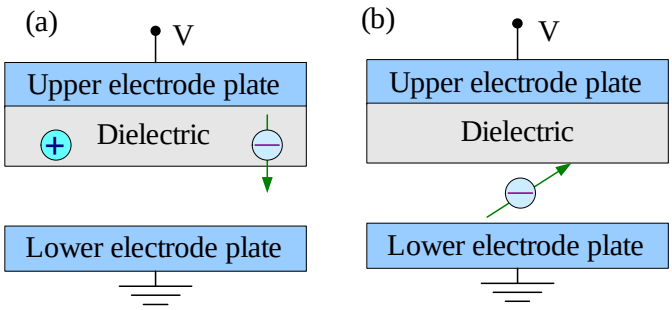

Figure 17. Illustration of the radiation effect on the charging mechanism.

(3) Breakdown voltage

For a long time the origin of electric breakdown has been considered to be different at the surface or in the bulk of dielectrics. The well-established Paschen's law relating the breakdown voltage of a gas in a uniform field with the product of the pressure p and the electrodes spacing d is used to state the breakdown characteristics of a gap [77,78]. Paschen's law reflects the Townsend breakdown mechanism and is usually written as

$$V_b = f(pd) = \frac{A_2 pd}{\ln(pd) + \ln\left[\frac{A_1}{\ln(1+1/\gamma)}\right]} \tag{27}$$

Where the constants A_1 and A_2 depend solely on the molecular properties of the gas, γ is the Townsend's ionization coefficient. For air, $A_1 = 15m^{-1}(Pa)^{-1}$, $A_2 = 365Vm^{-1}(Pa)^{-1}$ and $\gamma = 0.01$ [77]. The effect of the gap between electrodes, the shape of the electrodes, radiation, dust, temperature, and the packaging gas play important roles in determining the breakdown voltage.

The charge-to-failure model [73] was commonly applied to explain the dielectric breakdown. The dielectric resistance in a large electric field remains very high even though electrons and holes are injected. The charge carriers damage the dielectric, creating more defects and charge traps. Once a critical amount of charges have been accumulated, the dielectric will then be broken down. The well-known Paschen curve is often misrepresented when air gaps of the order of $5\mu m$ or less [73, 76]. The Paschen curve represents a gaseous breakdown model and predicts $360V$ as an absolute minimum value for a breakdown in air. This breakdown occurs at a gap of $8\mu m$, corresponding to a breakdown electric field of $4.5\times10^7 V/m$. For gaps smaller or larger than $8\mu m$, the Paschen curve predicts a breakdown voltage greater than $360V$. Shea et al. [73] illustrated that the modified Paschen curve was a good guide for choosing a safe operating range when scaling MEMS electrodes to gaps lower than $5\mu m$. However, it has been reported that the Paschen curve is not valid when the air gap between electrodes is less than $4\mu m$, where the breakdown voltage at this range is significantly less than that predicted by the Paschen curve [78, 79].The rapid fall-off breakdown voltage with the gap is associated with the presence of high electric fields ranging from $5\times10^7 V/m$ at $d = 0.25\mu m$ to $10^8 V/m$ at $d = 4\mu m$. The smallest potential difference measured in air is $12V$ at $d = 0.25\mu m$, which is about one thirtieth of

the minimum breakdown voltage according to Paschen's law. Moreover, Etching away the dielectric is a very effective solution to reduce the breakdown voltage, but not to damage the electrodes [73].

(4) Lifetime prediction

Since the high field strengths required for actuation of electrostatically actuated MEMS devices, the charging of the dielectrics become a more widespread problem. A typical dielectric of $200nm$ with a voltage of $40V$ across it will result in the field strength of $2\times10^8 V/m$ [72].

The critical amount of charge when actuating with a square wave can be obtained for different charge densities [80]. For the negative interface charge, the critical amount of charge σ_{crit} can be given by

$$\sigma_{crit} = -\sqrt{\frac{2\varepsilon_0 k(d-d_d)}{A}} \cdot \left[\frac{2\varepsilon_d(d-d_d)+d_d}{d_d}\right] \tag{28}$$

Zafar et al. [81] calculated the amount of parasitic charge after a certain charging period for thin high$-k$ gate dielectric stacks. The trapped charge density $\sigma(t)$ can be written as

$$\sigma(t) = N_0 q\left[1-\int_0^\infty \frac{\rho(\tau)}{N_0}\exp(-t/\tau)d\tau\right] \tag{29}$$

Where $\rho(\tau)$ is the charge distribution at the time τ, q is the elementary charge, t is the charging time, and N_0 is the total trap density.

When the amount of charge is so large that the pull-out voltage crosses zero, the device will fail [80]. The time constant for charging exponentially depends on the actuation voltage. Spengen et al. [80] simplified the trapped charge density $\sigma(t)$ and calculated the time to failure when $\sigma(t)=\sigma_{crit}$ for SiO_2 dielectric. The relationship between the actuation voltage V_a and the time to failure t_f can be yielded

$$t_f = -V_a Ln\left(\frac{\sigma_{crit}}{N_0 q}-1\right) \tag{30}$$

(5) Methods to reduce the effects of charging

Charging of the dielectrics and the associated uncertain electrostatic forces in MEMS structures have been a serious performance issue for many electrostatically actuated MEMS devices, such as microphones, displays, micromirrors, and RF switches, etc. [47,73-74]. Design, modeling and simulation that eliminate the effects of charging become more and more important.

Bochobza-Degani [61] modeled an interface charge and the modeling is too general to be easily applicable to real MEMS devices. A most straightforward method to decrease the effect of dielectric charging is to use a bipolar AC rather than DC voltage actuation [73]. However, the charging effect can not be eliminated completely and more complex actuation electronics are required. The other way to reduce the effect of the dielectric charging is by controlling the electrode and dielectric geometry, mainly the width of the gaps with exposed dielectric between electrodes, the thickness of the electrodes, selective etching of the dielectric and dielectric materials. Smaller gap can decrease the

magnitude of charging induced drift and shorten the saturation time, resulting in reducing the adverse effect of charging on mirror stability. At the same time, careful consideration of operating conditions and trade-off design are required before deciding on the ideal gap size for a given application due to the influences of the anodic oxidation and the breakdown voltage.

Moreover, depositing or growing a thin conductive layer on top of the dielectric in order both to bleed off surface charge and to screen bulk charge from the reflector has been developed and applied to MEMS devices [73]. This charge dissipation layer (CDL) must not contain charge traps and typically consists of a thin film of a poor conductor such as a doped oxide. A Co-Fe-O film of tunable conductance is an effective CDL for MEMS devices [73]. Rather than depositing a CDL over the dielectric, the dielectric material itself can act as a CDL if its electrical transport properties are suitable. For capacitive RF MEMS switches, Raytheon patented the approach of leaky SiN to control charging [82].

6.1.5. Environmentally induced failure mechanisms

(1) Anodic oxidation

Anodic oxidation of silicon electrodes and wiring is not a novel problem, but can be an important failure mode of non-hermetically packaging electrostatically actuated MEMS devices [73]. If moisture exists, the adsorbed water on the surface of the dielectric between electrodes or wiring provides a leakage path for current to flow between neighboring electrodes. Anodic oxidation in MEMS devices had been observed [83] and the effects (relative humidity, voltage, electric field, leakage current, and electrode geometry, etc.) of it on surface micromachined polisilicon had been performed [73,84]. Anodic oxidation occurs when there is a finite surface leakage current between electrodes on the surface of the dielectric. The poly-Si at the anode reacts with OH^- to form SiO_2 [85]. The rate of anodic oxidation is proportional to the leakage current between electrodes on the surface of the dielectric. Relative humidity is an accelerating factor, the higher the humidity, the more water is adsorbed on the surface, and thus the larger the surface leakage current will be. The surface leakage current increases roughly exponentially with relative humidity and the rate of anodic oxidation scales similarly with all other condition kept constant. Voltage is a strong accelerating factor because the leakage current is roughly proportional to the applied voltage. The electric field is also an accelerating factor. Much more oxidation is seen at sharp corners where the field is concentrated. Changing the gap between electrodes or wirings from 2 to $3\mu m$ has a large effect on the rate of anodic oxidation.

Shea et al. [73] illustrated two goals to control the rate of anodic oxidation. First, MEMS chips are designed such that anodic oxidation occurs as slowly as possible should the package leak. Second, structures that are purposefully extremely susceptible to anodic oxidation are designed and used as early warning devices.

(2) Electrostatic discharge

Electrostatic discharge (ESD) is an important consideration and has been observed as a failure mode in MEMS [65, 73]. An ESD discharge can cause both electrical and mechanical damage. Possible electrical damage from the discharge includes melted wires or electrodes, pinholes or weakened dielectrics, and shorted transistors. While the effects of ESD on MEMS structures have not been

published to date, it can be assumed that certain electrostatically actuated MEMS devices will be susceptible to the ESD damage.

6.2. Approaches to failure analysis

6.2.1. Selection of materials

The principal performance and reliability metrics considered for electrostatically actuated MEMS devices are the applied voltage, speed of actuation, actuation force, stored energy, electrical resistivity, mechanical quality factor, and resistance to fracture, friction, shock, and stiction [38, 40, 42, 86]. The materials properties governing these parameters are the Young's modulus, density, fracture strength, intrinsic residual stress, resistivity, and intrinsic material damping [38]. The material parameters of microstructures, such as Young's modulus and intrinsic stresses can also be given by the relationship between the electrostatic loads and the structural deflections [17].

According to the Ashby method for the selection of materials [87], the performance of an element can be described by the following form

$$p = p(F, G, M) \tag{31}$$

Where F, G and M represent the functional requirements, geometric parameters and material indices. p describes the performance aspects of component such as its mass or volume, cost and life. Optimal design is the selection of the material and geometry, maximizing or minimizing p according to its reliability and desirability.

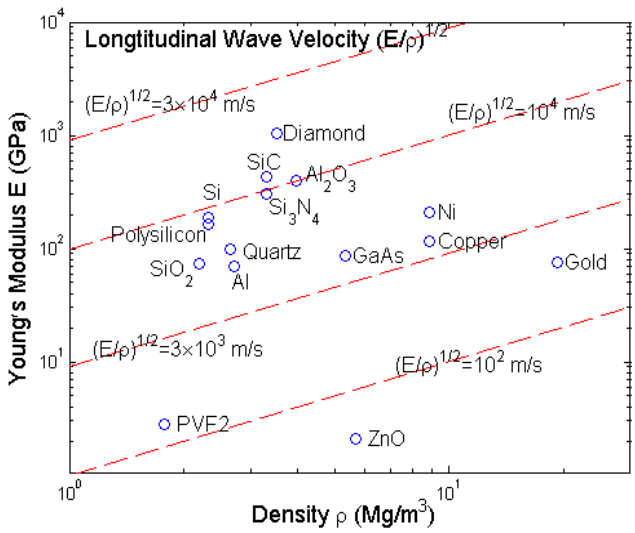

Figure 18. Materials selection chart with the Young's modulus plotted against the density on log scales, the log scales allow the longitudinal elastic wave velocity $v = (E/\rho)^{1/2}$ to be plotted as a set of parallel contours.

Skikar et al. [40] studied the properties of microfabrication structures and presented that the mass and inertial loads are material indices, i.e. density, bending stiffness is given by the Young's modulus, and the tip deflection is related to the maximum tensile stress (fracture strength). Many MEMS devices

are susceptible to the failure by electrostatically actuated stiction, which occurs when the structures are forced into mechanical contact at operation. The higher the bending stiffness, the lower the deflection and the probability of stiction will be. Requirements for the materials are that high $(E/\rho)^{1/2}$, low ρ and high E can be used to increase the probability of obtaining mechanical response, decrease the magnitude of the inertial load and minimize the structural deflection, respectively.

Fig. 18 plots the relationship between the Young's modulus E and the density ρ. Material performance indices for several elements are referred to the literatures [42]. It can be used to make an initial choice: diamond, silicon carbide (SiC), aluminum oxide (Al_2O_3), silicon nitride (Si_3N_4), and silicon (Si) emerge as the attractive candidates for fabricating electrostatically actuated MEMS devices with high resistance to stiction and adhesion.

The relationship between the Young's modulus E and the fracture strength σ_f is plotted in Fig. 19 for various microstructure materials. The nominal values shown in Fig. 19 are intended to guide the initial choice of materials. It is indicated that materials for the large force actuators are diamond, Al_2O_3 and SiC, etc.

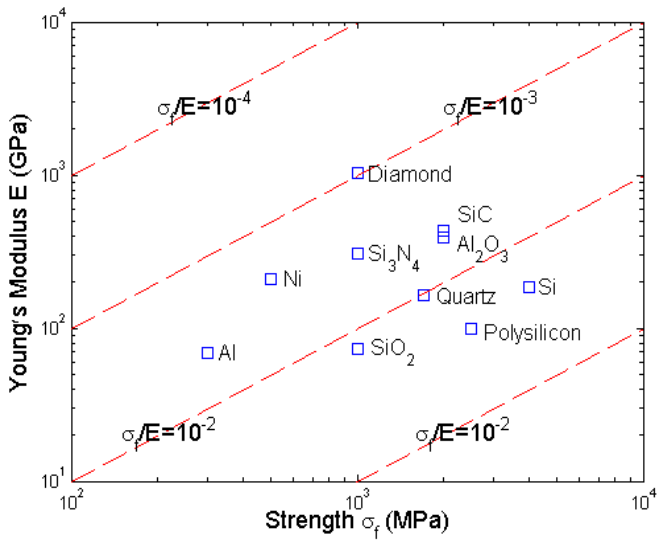

Figure 19. Materials selection chart with the Young's modulus plotted against the fracture strength.

Material properties may significantly affect the reliability of future products because MEMS designs become increasingly complex and the number of commercial applications is increasing [86]. Processing considerations have made silicon a popular choice as the material for the electrostatically actuated MEMS devices, but recent advances in micromachining techniques enable the integration of a number of different metals, alloys, ceramics, glasses, and polymers into MEMS [76]. For instance, the materials used to fabricate electrostatic micro-motors include silicon dioxide, nickel, diamond, silicon carbide, and polysilicon, etc. As the MEMS material sets continue to expand, it is necessary to find a rational and systematic approach to the selection of materials in the design of electrostatically actuated MEMS devices.

6.2.2. Modeling and simulation

The analysis of components in the MEMS design is often based on FEA. FEA is able to couple different physical domains (mechanical, thermal, electrical and piezoelectric, etc). In our previous work [88], the coupling effect of mechanical and piezoelectric domains on a micro-cantilever beam was studied and discussed. Part mode shapes of a beam (the length, width and thickness are $500\mu m$, $30\mu m$ and $3\mu m$ for a S_iO_2 beam, respectively) using finite element simulation are shown in Fig. 20.

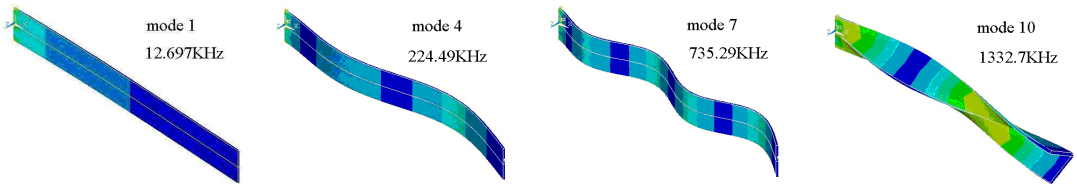

Figure 20. Part mode shapes of the beam using finite element simulation.

Although there are many designs which use piezoelectric, thermal and magnetic actuations, so far the most popular approach is to use electrostatic forces to move micromachined parts [33].The design of an electrostatically actuated device in MEMS is of great important. The fabrication of an electrostatic micro-actuator is becoming technologically feasible, but is extremely difficult, so that the mathematical modeling of the actuator design is likely to be very important in the advancement of this technology. Price et al [3] reviewed the basic elements of the electrostatic devices (conductors, dielectrics, insulators, electrets and ferroelectrics) and shown that the modeling of the electrostatic force is very different, and in many ways a more difficult undertaking than the modeling of a magnetic interaction. Models must take into account the realities of materials, in particular the fact that the resistivity is never infinite, and that any structural part of an actuator will affect fields through its dielectric.

Designs of MEMS devices which use the electrostatic forces as the actuated forces are complicated due to the fact that the dynamic characteristics of structure elements will be changed by the electrostatic forces and that as the structure deforms, the electrostatic forces redistribute, thereby modifying the mechanical loads [4]. Consequently, the structure-electrostatic coupling effect becomes an important issue on the design of such structures in MEMS.

Zhang et al. [37] presented a mathematic model and FE model to calculate the area of contact and stresses and strains in the contact region between the rotor and the bearing hub in an electrostatic micro-motor under the effect of electrostatic forces. The stress and strain distributions under different applied voltages are illustrated in Fig. 21 and Fig. 22. Fig. 21 shows the stress distributions in z direction at $U = 100V$. On the conditions of gap unchanged and maximum gap changed, the stresses are changing continuously. The maximum stresses are about $3.9\times10^6 N/m^2$ at $z = 0$ in z direction. In addition, the stresses in different scope and their distributions are similar to dissymmetrical and symmetrical ellipses. As shown in Fig. 22, the strains are symmetric concerning the axis and the distributions are close to half ellipses. The strains get the maximum values at $z = 0$, while obtaining the minimum at their maximum contact widths. Additionally, under different applied voltages, the strains are different and in direct proportion to the applied voltages, and similar to the stresses. When the rotor

bushing wears against the dielectric substrate, the gradient curve of the contact pressure distribution in the contact region can be illustrated in Fig. 23. The contact pressure displays an axis-symmetry parabolic distribution and the results satisfy the general rules of the theoretical solutions. It is indicated that the FE model is reasonable to model the contact behavior between the rotor bushing and the ground plane in electrostatic micromtors.

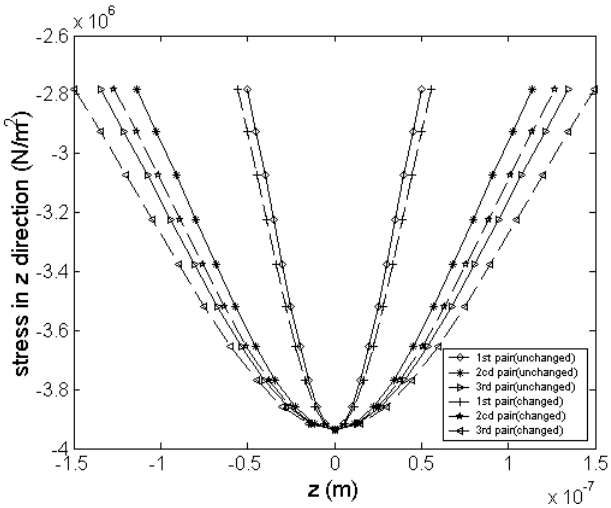

Figure 21. Stress distributions in z directions under the effect of gap ($U = 100V$).

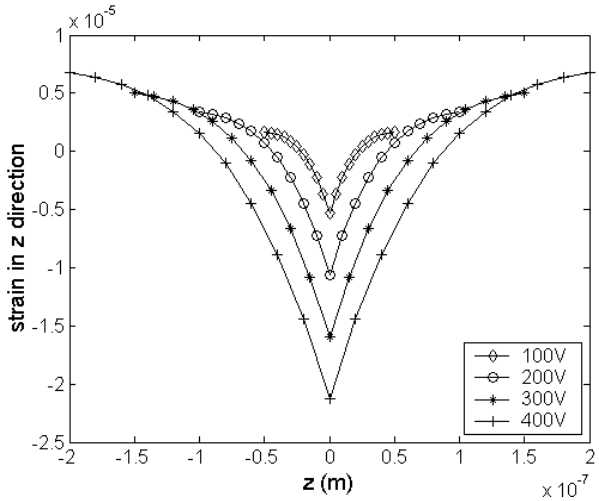

Figure 22. Strain distributions under different applied voltages.

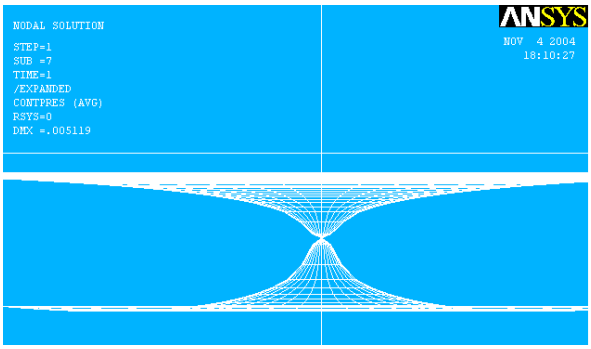

Figure 23. Gradient curve of contact pressure distribution in the contact region.

As driven systems, rotating electrostatic micro-motors are fabricated by surface micromachining using polysilicon with a thickness of only a few micrometers. Except for the reasonable design and effective modeling and simulation, many different microfabrication processes can then be applied for fabricating various electrostatic micro-motors. The polysilicon center pin process, polysilicon flange process, selective CVD tungsten process, Diamond-like Carbon (DLC) process, LIGA process with sacrificial layer, and three-mask tungsten process have been published for the fabrications of electrostatic micro-motors [13, 89].

In addition, Modeling and simulation of the electrostatically actuated MEMS devices play an important role in the design phase in predicting device characteristics [5]. For instance, the device models help the designers in identifying the regions of stable operation and in understanding the causes of instabilities.

6.2.3. Experimental techniques

This section focuses on the main experimental techniques that are suitable for studying the reliability of MEMS devices. The primary techniques, including observation, measurement and testing, are explained and discussed.

(1) Observation

Observation techniques are important to observe the contours, images, sizes, and arrangements of MEMS structures. Lafontan et al. [49] presented the conventional and new observation techniques, such as optical inspection (bright field illumination, dark field illumination and Normarsky contrast visualization), scanning electron microscopy (SEM), transmission electron microscopy (TEM), FIB-TEM, confocal IR imaging, and full field optical profilometer and vibrometer, etc. FIB, parallel polishing, lift-off and laser ablation have been developed and applied to MEMS sample preparations.

FIB preparation uses the ion beam to image the sample and to remove material from both sides of the desired section [49, 69, 72, 90]. In the FIB, the material removal is monitored in real time. Pre-thinning and lift out are the two approaches to FIB sample preparations and the cross-section of an unreleased electrostatic micro-motor realized in MUMPs [49, 90]. In such a design, the size of the oxide layers controls the mechanical clearance between the rotor and the hub. The gap between the rotor and the hub is approximately 15% thinner than the standard layer thickness. It is important for the designer to calculate the capacitive electrostatic force with this gap.

(2) Measurement

In recent years, many measurement methods and instruments have been developed and used to MEMS devices [49, 66, 80, 91]. For the measurement, contact, non-contact and an intermediate mode are the main methods [49]. The surface roughness of MEMS structure can be measured using atomic force microscopy (AFM). The optical scanning profilometer can measure the topography in 3D of a surface and its roughness with non-contact [49]. SEM and AFM can be used to measurement the stiction characterizations of MEMS structures, such as RF MEMS switch [66, 80].

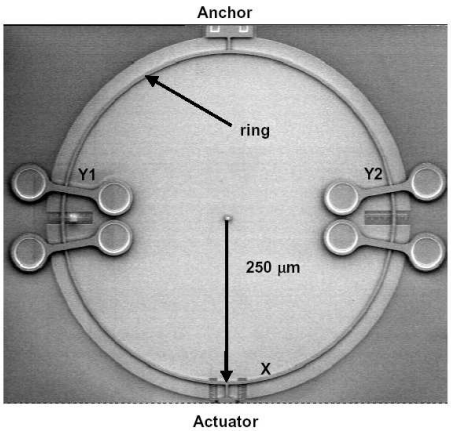

(*Courtesy of D.M. Tanner*)

Figure 24. SEM image of the force detector shows the ring and the location of the anchor and actuator, the force detector ring has gages at the three locations of X, Y1, and Y2 [91].

In order to characterize an electrostatic actuator, the spring constant and force output of the actuator must be determined. Bending equations are then used to calculate the force. Tanner et al. [91] described a novel force detector used to determine force and spring constant. The force detector contains a ring of polysilicon anchored to the substrate at one location and attached to the actuator 180° from the anchor as shown in Fig. 24. Pulling from the actuator end will elongate the ring, with deflections measured in three locations (X, Y1, and Y2).

(3) Testing

In order to get the failure data from the electrostatically actuated MEMS devices, many testing methods have been presented and test vehicles have been designed [71-72, 92-93]. A popular way to obtain fatigue data is the resonant aging method. The main wear mechanism was investigated by a Sandia electrostatic micro-motor [72]. Ashursta et al. [92] successfully designed, fabricated and tested a functional first generation electrostatic sidewall adhesion test device. Larsen et al. [93] developed a representative fatigue testing device. In the top part of the testing beam and the corresponding lever arm is situated. The right hand side of the lever is connected to the electrostatic actuator in the bottom part via the narrow flexible beam. The electrostatic actuator operates by pull-in of the moveable electrodes. The device uses two sets of electrodes. Bumpers stop the electrodes before short circuit, leaving a $2\mu m$ gap. Using direct electrostatic plate-to-plate attraction yields larger attraction forces per device area compared to the comb devices, by which the size and complexity of the component is reduced.

7. Conclusions

Electrostatic forces of importance and necessary in MEMS are investigated and analyzed in this paper. It is shown that because of extremely small sizes of microstructures in MEMS, interaction between micromechanical components caused by electrostatic forces may become significant to influence the behaviors of MEMS devices.

Electrostatic forces display many advantages than other actuated forces due to the scaling effect, an electrostatic micro-actuator is suitable for micro-sensors and micro-actuators and is easy to miniaturize. However, pull-in instability and many influence factors restrict the wide applications of the electrostatically actuated MEMS devices, and nonlinear effects due to electrostatic forces also affect the dynamic characteristics and reliability of the electrostatically actuated MEMS components or even the whole dynamic systems.

In conclusion, the research on the interaction of stability, nonlinearity and reliability in the electrostatically actuated MEMS devices is an interesting and significant field of very importance for the successful applications of MEMS technology. It is necessary to develop new solution methods and novel techniques to meet the requirements for further investigating the interplay and coupling of stability, nonlinearity and reliability in MEMS.

Acknowledgements

The authors are grateful to Dr. J. Y. Chen and J. B. Zhou for their valuable suggestions. This work was supported by the National Natural Science Foundation of China under Grant No. 10602033 and 50575132, the National Outstanding Youth Foundation of China under Grant No.10325209, and the China Postdoctoral Science Foundation under Grant No. 20060400165.

References

1. Huber, J.E.; Fleck, Z.A.; Ashby, M.F. The selection of mechanical actuators based on performance indices. *Proc R Soc London Ser A* **1997**, *453*, 2185-2205.
2. Zhou, Shu-Ang. On forces in microelectromechanical systems. *International Journal of Engineering Science* **2003**, *41*, 313-335.
3. Price, R.H.; Wood, J.E; Jacobsen, S.C. Modelling considerations for electrostatic forces in electrostatic microactuators. *Sensors and Actuators* **1989**, *20*, 107-114.
4. Hu, Y.C.; Chang, C.M.; Huang, S.C. Some design considerations on the electrostatically actuated microstructures. *Sensors and Actuators A* **2004**, *112*, 155-161.
5. Pamidighantam, S.; Puers, R.; Baert, K.; Tilmans, H.A.C. Pull-in voltage analysis of electrostatically actuated beam structures with fixed-fixed and fixed-free end conditions. *J Micromech Microeng* **2002**, *12*, 454-464.
6. Sasayama, T.; Suzuki, S.; Tsuchitani, S.; Koide, A.; Suzuki, M.; Ichikawa, N.; Nakazawa, T. Highly reliable silicon micromachined physical sensors in mass production. *Sensors and Actuators A* **1996**, *54*, 714-717.
7. Bao, M.H.; Yang, H.; Yin, H.; Shen, S.Q. Effects of electrostatic forces generated by the driving signal on capacitive sensing devices. *Sensors and Actuators A* **2000**, *24*, 213–219.
8. Lee, S.; Ramadoss, R.; Buck, M.; Bright, V.M.; Gupta, K.C.; Lee, Y.C. Reliability testing of flexible printed circuit-based RF MEMS capacitive switches. *Microelectronics Reliability* **2004**, *44*, 245–250.
9. MoCarthy, B.; Adams, G.G.; McGruer, N.E.; Potter, D. A dynamical model, including contact bounce, of an electrostatically actuated microswitch. *J Microelectromech Syst* **2002**, *11*, 276-283.
10. Millet, O.; Bernardoni, P.; Regnier, S.; Bidaud, P.; Tsitsiris, E.; Collard, D.; Buchaillot, L.

Electrostatic actuated micro gripper using an amplification mechanism. *Sensors and Actuators A* **2004**, *114*, 371-378.

11. Schiele, I.; Huber, J.; Hillerich, B.; Kozlowski, F. Surface-micromachined electrostatic microrelay. *Sensors and Actuators A* **1998**, 66, 345-354.
12. Mehregany, M.; Nagarkar, P.; Senturia, S.D.; Lang, J.H. Operation of microfabricated harmonic and ordinary side-drive motors. Proc. 3rd. IEEE MEMS Workshop, Napa Valley, CA, Feb. **1990**. p. 1–8.
13. Tavrow, L.S.; Bart, S.F.; Lang, J.H. Operational characteristics of microfabricated electric motors. *Sensors and Actuators A* **1992**, *35*, 33-44.
14. Ishihara, H.; Arai, F.; Fukuda. T. Micro mechatronics and micro actuators. *IEEE/ASME Transactions on Mechatronics* **1996**, *1(1)*, 68-79.
15. Zhang, W.M.; Meng, G.; Li, H.G. Electrostatic micromotor and its reliability. *Microelectronics Reliability* **2005**, *45*, 1230-1242.
16. Hung, E.S.; Senturia, S.D. Extending the travel range of analog-tuned electrostatic actuators. *J Microelectromech Syst* **1999**, *8(4)*, 497-505.
17. Osterberg, P.M.; Senturia, S.D. M-test: a test chip for MEMS material property measurement using electrostatically actuated test structures. *J Microelectromech Syst* **1997**, *6(2)*, 107–118.
18. Zhang, W.M.; Meng G. Nonlinear dynamic analysis of electrostatically actuated resonant MEMS sensors under parametric excitation. *IEEE Sensors Journal* **2007**, 7(3), 370-380.
19. Castaner, L.M.; Senturia, S.D. Speed-energy optimization of electrostatic actuators based on pull-in. *J Microelectromech Syst* **1999**, *8*, 290-298.
20. Castaner, L.; Rodriguez, A.; Pons, J.; Senturia, S.D. Pull-in time energy product of electrostatic actuators: comparison of experiments with simulation. *Sensors and Actuators A* **2000**, *83*, 263-269.
21. Quevy, E.; Bigotte, P.; Collard, D.; Buchaillot, L. Large stroke actuation of continuous membrane for adaptive optics by 3D self-assembled microplates. *Sensors and Actuators A* **2002**, *95*, 183-195.
22. Chan, E.K.; Dutton, R.W. Electrostatic micromechanical actuator with extended range of travel. *J Microelectromech Syst* **2000**, *9*, 321-328.
23. Nadal-Guardia, R.; Dehe, A.; Aigner, R.; Castaner, L.M. Current drive methods to extend the range of travel of electrostatic microactuators beyond the voltage pull-in point. *J Microelectromech Syst* **2002**, *11*, 255-263.
24. Legtenberg, R.; Gilbert, J.; Senturia, S.D.; Elwenspoek, M. Electrostatic curved electrode actuators. *J Microelectromech Syst* **1997**, *6*, 257-265.
25. Tang, W.C.; Nguyen, T.C.H.; Judy, M.W.; Howe, R.T. Electrostatic comb drive of lateral polysilicon resonators. *Sensors and Actuators A* **1990**, *21-23*, 323-331.
26. Ye, W.; Mukherjee, S.; Macdonald, N.C. Optimal shape design of an electrostatic comb drive in microelectromechanical systems. *J Microelectromech Syst* **1998**, *7*, 16-26.
27. Busta, H.; Amantea, R.; Furst, D.; Chen, J.M.; Turowski, M.; Mueller, C. A MEMS shield structure for controlling pull-in forces and obtaining increased pull-in voltages. *J Micromech Microeng* **2001**, *11*, 720-725.

28. Zhang, W.M.; Meng, G. Nonlinear dynamical system of micro-cantilever under combined parametric and forcing excitations in MEMS. *Sensors and Actuators A* **2005**, *119*, 291-299.
29. Liu, S.; Davidson, A.; Lin, Q. Simulating nonlinear dynamics and chaos in a MEMS cantilever using Poincare mapping. IEEE, Transducers'03, the 12th International Conference on Solid State Sensors, Actuators and Microsystems, Boston, June 8-12, **2003**. pp.1092-1095.
30. Adams, S.G.; Bertsch, F.M.; Shaw, K.A.; MacDonald, N.C. Independent tuning of linear and nonlinear stiffness coefficients. *J Microelectromech Syst* **1998**, *7(2)*, 172-180.
31. Zhang, W.; Baskaran, R.; Turner, K.L. Effect of cubic nonlinearity on auto-parametrically amplified resonant MEMS mass sensor. *Sensors and Actuators A* **2002**, *102*, 139–150.
32. Li, G.; Aluru, N.C. Linear, nonlinear and mixed-regime analysis of electrostatic MEMS. *Sensors and Actuators A* **2001**, *91*, 278-291.
33. Aluru, N.R.; White, J. An efficient numerical technique for electromechanical simulation of complicated microelectromechanical structures. *Sensors and Actuators A* **1997**, *58*, 1-11.
34. Younis, M.I.; Abdel-Rahman, E.M.; Nayfeh, A. A reduced-order model for electrically actuated microbeam-based MEMS. *J Microelectromech Syst* **2003**, *12(5)*, 672-680.
35. Senturia, S.D.; Harris, R.M.; Johnson, B.P.; Kim, S.; Nabors, K.; Shulman, M.A.; White, J.K. A computer-aided design system for microelectromechanical systems (MEMCAD). *J Microelectromech Syst* **1992**, *1*, 3–13.
36. Li, G.Y.; Wang, L. Influence of bonding parameters on electrostatic force in anodic wafer bonding. *Thin Solid Films* **2004**, *462–463*, 334–338.
37. Zhang, W.M.; Meng, G. Contact dynamics between the rotor and bearing hub in an electrostatic micromotor. *Microsystem Technologies* **2005**, *11*, 438–443.
38. Srikar, V.T.; Spearing, S.M. Materials selection for microfabricated electrostatic actuators. *Sensors and Actuators A* **2003**, *102*, 279-285.
39. Zhang, W.M.; Meng, G. Stability, bifurcation and chaos analyses of a high-speed micro-rotor system with rub-impact. *Sensors and Actuators A: Physical* **2006**, *127(1)*, 163-178.
40. Srikar, V.T.; Spearing, S.M. Materials selection in micromechanical design: an application of the Ashby approach. *J Microelectromech Syst* **2003**, *12(1)*, 3-10.
41. Zhang, W.M.; Meng, G. Numerical simulation of sliding wear between the rotor bushing and ground plane in micromotors. *Sensors and Actuators A: Physical* **2006**, *126*, 15-24
42. Spearing, S.M. Materials issues in microelectromechanical systems (MEMS). *Acta mater* **2000**, *48*, 179-196.
43. Li, B.Q.; Zhu, C.C.; Liu, J.H. Electrostatic force influenced by space charge in submicrometer or nanometer silicon microstructures. *J Micromech Microeng* **1999**, *9*, 319–323.
44. Trimmer, W.S.N. Microrobots and Micromechanical Systems. *Sensors and Actuators* **1989**, *19(3)*, 267-287.
45. Peirs, J.; Reynaerts, D.; Brussel, H.V. Scale effects and thermal considerations for micro-actuators. Proceedings of the 1998 IEEE International Conference on Robotics & Automation, Leuven, Belgium, May **1998**. p. 1516-21.

46. Fischer, M.; Giousouf, M.; Schaepperle, J.; Eichner, D.; Weinmann, M. Electrostatically deflectable polysilicon micromirrors-dynamic behaviour and comparison with the results from FEM modeling with ANSYS. *Sensors and Actuators A* **1998**, *67*, 89-95.
47. Wibbeler, J.; Pfeifer, G.; Hietschold, M. Parasitic charging of dielectric surfaces in capacitive microelectromechanical systems (MEMS). *Sensors and Actuators A* **1998**, *71(1-2)*, 74-80.
48. O'Mahony, C.; Duane, R.; Hill, M.; Mathewson, A. Low-voltage micromechanical test structures for measurement of residual charge in dielectrics. *Electronics Letters* **2005**, *41(7)*, 409-410.
49. Lafontan, X.; Pressecq, F.; Beaudoin, F.; Rigo, S.; Dardalhon, M.; Roux, J.-L.; Schmitt, P.; Kuchenbecker, J.; Baradat, B.; Lellouchi, D.; Le-Touze, C.; Nicot, J.-M. The advent of MEMS in space. *Microelectronics Reliability* **2003**, *43*, 1061-1083.
50. Rocha, L.A.; Cretu, E.; Wolffenbuttel, R.F. Full characterization of pull-in single-sided clamped beams. *Sensors and Actuators A* **2004**, *110*, 301-309.
51. Rocha, L.A.; Cretu, E.; Wolffenbuttel, R.F. Compensation of temperature effects on the pull-in voltage of microstructures. *Sensors and Acutators A* **2004**, *115*, 351-356.
52. Rocha, L.A.; Cretu, E.; Wolffenbuttel, R.F. The pull-in of symmetrically and asymmetrically driven microstructures and the use in dc voltage references. In Proc. of IMTC02, Vol. 1, Anchorage, USA, 21-23 May **2002**. pp. 759-764.
53. Tada, H.; Kumpel, A.E.; Lathrop R.E.;Slanina, J.B.; Nieva, P.; Zavracky, P.; Miaoulis, I.N.; Wong, P.Y. Thermal expansion coefficient of polycrystalline silicon and silicon dioxide thin films at high temperatures. *J Appl Phys* **2000**, *87*, 4189-4193.
54. Burns, D.M.; Bright, V.M. Nonlinear flexture for stable deflection of an electrostatically actuated micromirror. In Proc. of the SPIE on Microelectronics Structures and MEMS for Optical Processing , Vol.3226, **1997**. pp. 125-135.
55. Rosa, M.A.; Bruyker, D.D.; Volkel, A.R.; Peeters, E. A novel external electrode configuration for the electrostatic actuation of MEMS based devices. *J Micromech Microeng* **2004**, *14*, 446-451.
56. Seeger, J.I.; Boser, B.E. Dynamics and control of parallel-plate actuators beyond the electrostatic instability. In: Proc. of the Transducers, **1999**. pp. 474-477.
57. Chu, P.B.; Pister, K.S.J. Analysis of closed-loop control of parallel plate electrostatic microgrippers. In: Proc. of the IEEE International Conference on Robotics and Automation **1994**; pp. 820-825.
58. Sun, Y.; Piyabongkarn, D.; Sezen, A.; Nelson, B.J.; Rajamani, R. A high-aspect-ratio two-axis electrostatic microactuator with extended travel range. *Sensors and Actuators A* **2002**, *102*, 49-60.
59. Gilbert, J.R.; Senturia, S.D. Two-phase actuators: stable zipping devices without fabrication of curved structures Solid-State Sensor and Actuator Workshop (Hilton Head, SC) **1996**; pp 98–100.
60. Legtenberg, R.; Berenschot, E.; Elwenspoek, M.; Fluitman, J. Electrostatic curved electrode actuators. IEEE Workshop on Micro Electro Mechanical Systems (MEMS)'95, Amsterdam, **1995**; pp. 37–42.
61. Bochobza-Degani, O.; Elata, D.; Nemirovsky, Y. A general relation between the ranges of stability of electrostatic actuators under charge or voltage control. *Appl Phys Lett* **2003**, *82*, 302–304.
62. Chu, P.B. ; Nelson, P.R. ; Tachiki, M.L. ; Pister, K.S. Dynamics of polysilicon parallel-plate electrostatic actuator. *Sensors and Actuators A* **1996**, *52*, 216-220.

63. Veijola, T.; Kuisma, H.; Lahdenpera, J. The influence of gas-surface interaction on gas film damping in a silicon accelerometer. *Sensors and Actuators A* **1998**, *66*, 83-92.
64. Starr, J.B. Squeeze-film damping in solid-state accelerometers, Proc. IEEE Solid State Sensor and Actuator Workshop, Hilton Head Island, SC, USA, June4-7, **1990**. pp.44-47.
65. Walraven, J.A. Failure Mechanisms in MEMS. ITC International Test Conference. Charlotte, NC, USA, September 30-October 02, **2003**. pp. 808-812.
66. Spengen, W.M.V.; Puers, R.; Wolf, I.D. A physical model to predict stiction in MEMS. *J Micromech Microeng* **2002**, *12*, 702-713.
67. Knudson, A.R.; Buchner, S.; McDonald, P.; Stapor, W.J.; Campbell, A.B.; Grabowski, K.S.; Knies, D.L.; Lewis, S.; Zhao, Y. The effects of radiation on MEMS accelerometers. IEEE Trans Nucl Sci Indian Wells, CA, USA, **1996**; 43(6):3122-3126.
68. Gabriel, K.J.; Behi, F.; Mahadevan, R. In-Situ Friction and Wear Measurements in Integrated Polysilicon Mechanisms. *Sensors and Actuators A* **1990**, *21-23*, 184-188.
69. Tanner, D.M.; Miller, W.M.; Peterson, K.A.; Dugger, M.T.; Eaton, W.P.; Irwin, L.W.; Senft, D.C.; Smith, N.F.; Tangyunyong, P.; Miller, S.L. Frequency dependence of the lifetime of a surface micromachined microengine driving a load. *Microelectronics Reliability* **1999**, *39*, 401-414.
70. Kahn, H.; Tayebi, N.; Ballarini, R.; Mullen, R.L.; Heuer, A.H. Fracture toughness of polysilicon MEMS devices. *Sensors and Actuators A* **2000**, *82*, 274-280.
71. Komvopoulos, K. Surface engineering and microtribology for microelectromechanical systems. *Wear* **1996**, *200(1-2)*, 305-327.
72. Spengen, W.M.V. MEMS reliability from a failure mechanisms perspective. *Microelectronics Reliability* 2003, *43*, 1049-1060.
73. Shea, H.R.; Gasparyan, A.; Chan, H.B.; Arney, S.; Frahm, R.E.; Lopez, D.; Jin, S.; McConnel, R.P. Effects of electrical leakage currents on MEMS reliability and performance. *IEEE Transactions on Device and Materials Reliability* **2004**, *4(2)*, 198-207.
74. Schanwald, L.P.; Schwank, J.R.;Sniegowski, J.J.; Albuquerque, N.M. Radiation effects on surface micromachined comb drives and microengines. *IEEE Trans Nucl Sci* **1998**, *45*, 2789-2798.
75. Mcclure, S.S.; Edmonds, L.D.; Mihailovich, R.; Johnston, A. Radiation effects in microelectromechanical systems (MEMS): RF relay. *IEEE Transactions on Nuclear Science* **2002**, *49(6)*, 3197-3202.
76. Madou, M.J. Fundamentals of Microfabrication: The Science of Miniaturization, 2nd ed. Cleveland, OH: CRC Press; **2002**.
77. http://home.earthlink.net/~jimlux/hv/paschen.htm (online)
78. Dhariwal, R.S.; Torres, J.M.; Desmulliez, M.P.Y. Electric field breakdown at micrometer separations in air and nitrogen at atmospheric pressure. *IEE Proc Sci Meas Technol* **2000**, *147(5)*, 261-265.
79. Torres, J.M.; Dhariwal, R.S. Electric field breakdown at micrometre separations in air and vacuum. *Microsystem Technologies* **1999**, *6*, 6-10.

80. Spengen, W.M.V.; Puers, R.; Mertens, R.; Wolf, I.D. A comprehensive model to predict the charging and reliability of capacitive RF MEMS switches. *J Micromech Microeng* **2004**, *14*, 514-521.
81. Zafar, S.; Callegari, A.; Gusev, E.; Fischetti, M.V. Charge trapping in high k gate dielectric stacks. Proc Int Electron Devices Meeting (IEDM) **2002**, pp.517.
82. Ehmke, J.; Goldsmith, C.; Yao, Z.; Eshelman, S. Method and apparatus for switching high frequency signals. U.S. Patent 6, 391, 675, May 21 **2002**.
83. Shea, H.R.; White, C.; Gasparyan, A.; Comizzoli, R.B.; Abusch-Magder, C.; Arney, S. Anodic oxidation and reliability of poly-Si MEMS electrodes at high voltages and in high relative humidity. MEMS Reliability for Critical Applications, R. Lawton, Ed., **2000**, vol. 4180, Proc. SPIE; p. 117–122.
84. Plass, R.A.; Walraven, J.A.; Tanner, D.M.; Sexton, F.W. Anodic oxidation-induced delamination of the SUMMiT polysilicon nitride interface. Reliability, Testing, and Characterization of MEMS/MOEMS II, R. Ramesham and D. M. Tanner, Eds., **2003**, vol. 4980, Proc. SPIE; p. 81–86.
85. Lewerenz, H.J. Anodic oxides on silicon. *Electrochimica Acta* **1992**, *37*, 847–864.
86. Romig, J.A.D.; Dugger, M.T.; McWhorter, P.J. Materials issues in microelectromechanical devices: science, engineering, manufacturability and reliability. *Acta Materialia* **2003**, *51*, 5837-5866.
87. Ashby, M.F. Materials Selection in Mechanical Design. Oxford, U.K.: Butterworth-Heinemann; **1999**.
88. Zhang, W.M.; Meng, G. Active vibration control of micro-cantilever beam in MEMS. IEEE, International Conference on Intelligent Mechatronics and Automation, Chengdu, China, August 26-31 **2004**. pp. 272-276.
89. Zettler, T. Integrated circuit fabrication compatible three-mask tungsten process for micromotors and gears. *Sensors and Actuators A* **1994**, *44*, 159-163.
90. Reyntjens, S.; Puers, R. A review of focused ion beam applications in microsystem technology. *J Micromech Microeng* **2001**, *11*, 287–300.
91. Walraven, J.A.; Peterson, K.A.; Tangyunyong, P.; Dugger, M.T.; Miller, S.L. MEMS reliability: Infrastructure, test structures, experiments, and failure modes. Sandia National Laboratories, Albuquerque, NM, Sandia Rep. SAND **2000**-0091.
92. Ashursta, W.R.; Boerb, M.P.D.; Carraroa, C.; Maboudian, R. An investigation of sidewall adhesion in MEMS. *Applied Surface Science* **2003**, *212-213*, 735-741.
93. Larsen, K.P.; Rasmussen, A.A.; Ravnkilde, K.T.; Ginnerup, M.; Hansen, O. MEMS device for bending test: measurements of fatigue and creep of electroplated nickel. *Sensors and Actuators A* **2003**, *103*, 156-164.